Coupled ocean/sea ice dynamics of the Antarctic Slope Current driven by topographic eddy suppression and sea ice momentum redistribution

Yidongfang Si,[a] Andrew L. Stewart,[a] Ian Eisenman,[b]

[a] *Department of Atmospheric and Oceanic Sciences, University of California, Los Angeles, Los Angeles, California*
[b] *Scripps Institution of Oceanography, University of California, San Diego, La Jolla, California*

ABSTRACT: The Antarctic Slope Current (ASC) plays a central role in redistributing water masses, sea ice, and tracer properties around the Antarctic margins, and in mediating cross-slope exchanges. While the ASC has historically been understood as a wind-driven circulation, recent studies have highlighted important momentum transfers due to mesoscale eddies and tidal flows. Furthermore, momentum input due to wind stress is transferred through sea ice to the ASC during most of the year, yet previous studies have typically considered the circulations of the ocean and sea ice independently. Thus it remains unclear how the momentum input from the winds is mediated by sea ice, tidal forcing, and transient eddies in the ocean, and how the resulting momentum transfers serve to structure the ASC. In this study the dynamics of the coupled ocean/sea ice ASC circulation are investigated using high-resolution process-oriented simulations, and interpreted with the aid of a reduced-order model. In almost all simulations considered here, sea ice redistributes almost 100% of the wind stress away from the continental slope, resulting in approximately identical sea ice and ocean surface flows in the core of the ASC in a fully spun-up equilibrium state. This ice-ocean coupling results from suppression of vertical momentum transfer by mesoscale eddies over the continental slope, which allows the sea ice to accelerate the ocean surface flow until the speeds coincide. Tidal acceleration of the along-slope flow exaggerates this effect, and may even result in ocean-to-ice momentum transfer. The implications of these findings for along- and across-slope transport of water masses and sea ice around Antarctica are discussed.

1. Introduction

The Antarctic Slope Current (ASC) is a westward narrow and swift circulation that surrounds the Antarctic margins. The ASC is important for the climate system and biogeochemistry, as it forms a barrier for the cross-slope exchanges such as heat, freshwater, nutrients and biota between the Antarctic continental shelf and the open ocean (Jacobs 1991; Whitworth et al. 1985; Heywood et al. 2014). Fig. 1d shows the winter climatology of sea surface elevation, with the ASC sketched by the gray arrow. In the regions where the ASC is weaker (denoted by the dashed gray arrow in Fig. 1d), warm deep water is able to intrude onto the continental shelf, causing enhanced melting of Antarctic ice shelves (Thompson et al. 2018). The zonal flow of the ASC is an important conduit for the transport of water masses, tracers, sea ice and icebergs around Antarctica (Heywood et al. 1998; Stern et al. 2016).

The surface winds close to the Antarctic margins are mostly parallel to the coastline and directed westward all year round (Powers et al. 2003, 2012; Hazel and Stewart 2019), with speeds that decrease offshore and drive shoreward Ekman transport (Gill 1973; Heywood et al. 2014). These winds play an important role in the overturning circulation and cross-slope transport near the continental shelf and slope (Stewart and Thompson 2013, 2015; Goddard et al. 2017). As a main source of momentum input to the ice and ocean system, surface wind stress has been suggested as having a leading-order impact on the mean transport and seasonal and interannual variability of the ASC (Mathiot et al. 2011; Armitage et al. 2018; Naveira Garabato et al. 2019). The winter zonal wind speed is shown in Fig. 1a. In addition to winds, buoyancy forcing has been regarded as an important driver of the ASC (Hattermann 2018; Thompson et al. 2020). Using a high-resolution global ocean-sea ice model, Moorman et al. (2020) have shown that the intensity and spatial pattern of the ASC are substantially modified by coastal freshening, as is projected to occur due to increased ice sheet melt over the coming centuries (Naughten et al. 2018). However, the role of buoyancy forcing in the ASC circulation is less well understood because the observations of buoyancy forcing near the Antarctic margins are spatially and temporally sparse.

Though wind and buoyancy forcings have historically been implicated as key drivers of the ASC (Jacobs 1991; Whitworth et al. 1985), recent studies have increasingly suggested that high-frequency variability associated with eddies, tides and dense outflows may be critical to the along-slope circulation and cross-slope exchange (Thompson et al. 2018). Eddies are generated by barotropic and baroclinic instabilities of the ASC (Stewart and Thompson 2016; Stewart et al. 2019), and vorticity conservation of dense outflows (Spall and Price 1998; Wang et al. 2009). Previous studies have identified mesoscale eddies as a major contributor to the onshore transport of the circumpolar deep water (CDW) (Nøst et al. 2011; Thompson et al. 2014; Stewart and Thompson 2015) and the offshore export of the Antarctic Bottom Water (AABW) (Wang et al. 2009; Nakayama et al. 2014; Stewart and Thompson 2015).

Corresponding author: Yidongfang Si, csi@atmos.ucla.edu

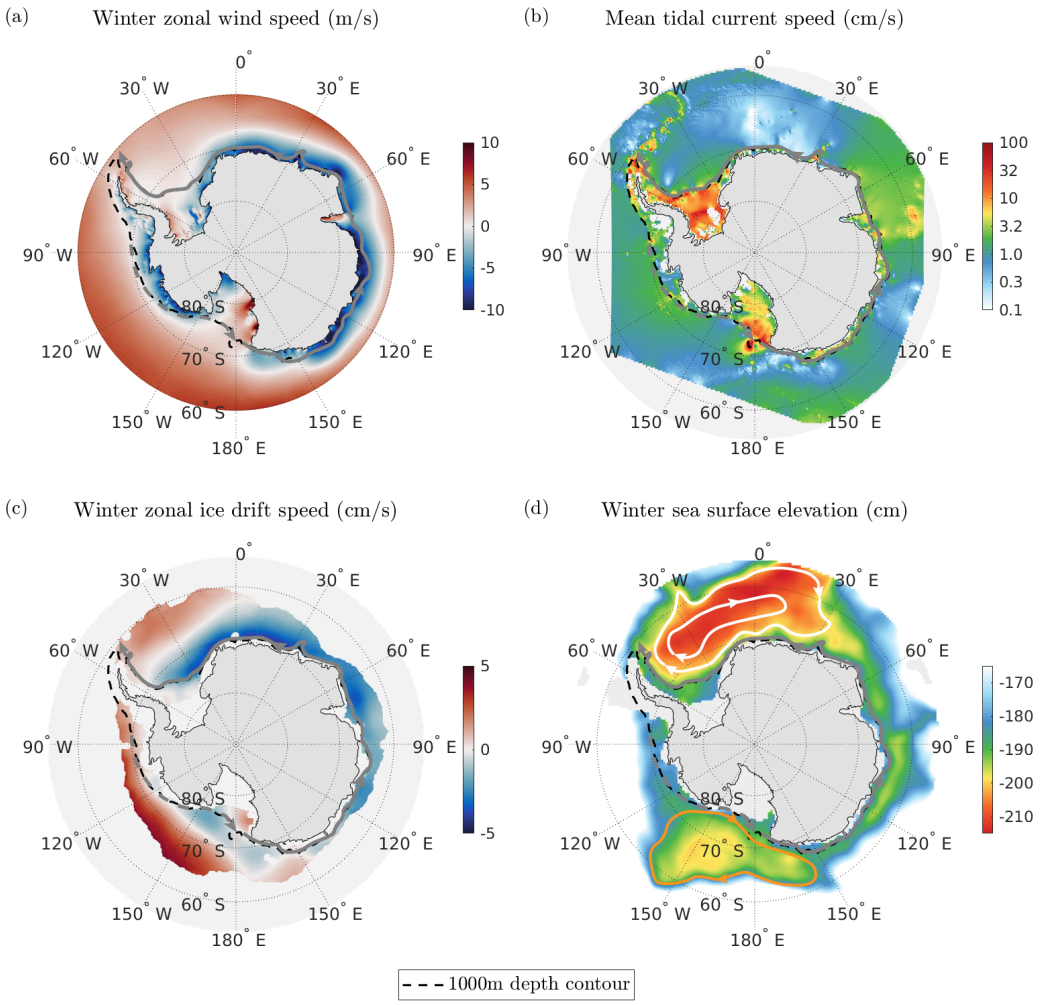

Figure 1. The observed external forcing of the sea ice-ocean system around the Antarctic margin, and the motion of the sea ice and the ocean in the Antarctic winter. (a) The winter (June, July, and August) climatology of zonal wind speed from 2007-2014, using the Antarctic Mesoscale Prediction System (AMPS) products (Powers et al. 2003, 2012). (b) The annual average of tidal current speed including ten major tidal constituents, calculated by the model CATS2008 (Padman et al. 2002, 2008). (c) The winter climatology of zonal ice drift speed from 1979-2015, using the product "Polar Pathfinder Daily 25 km EASE-Grid Sea Ice Motion Vectors, Version 3" (Tschudi et al. 2016). (d) The winter climatology of sea surface elevation using the Dynamic Ocean Topography (DOT) data (Armitage et al. 2018). The gray, white, and orange curved arrows denote the Antarctic Slope Current, the Weddell Gyre, and the Ross Gyre with their directions, respectively. The black dashed curve around the Antarctic continent represents the 1000m isobath.

Mesoscale eddies are also shown to produce rectified mean along-slope flows (McWilliams 2008; Wang and Stewart 2018; Cherian and Brink 2018). Eddies may play a key role in the momentum balance of major current systems: the isopycnal form stress arising from transient and standing eddies is the primary mechanism of vertical momentum transfer in the Southern Ocean (Tréguier and McWilliams 1990; Masich et al. 2018). We might expect similar dynamics to take place in the ASC. However, over the continental slope the tracer transport and momentum fluxes carried by mesoscale eddies are greatly reduced, because the baroclinic instability may be suppressed by topographic vorticity gradient (Blumsack and Gierasch 1972; Isachsen 2011; Hetland 2017). The suppression of eddy fluxes over the slope has been invoked to explain the "V-shaped" isopycnals of the Antarctic Slope Front (ASF) in the AABW formation region (Stewart and Thompson 2013). Yet it is still unclear how eddies mediate momentum input due to wind stress in the ASC under sea ice cover.

In addition to mesoscale eddies, tides are key contributors to the circulation around Antarctic margins (Thompson et al. 2018), and have an impact on water mass ex-

change and transformation (Muench et al. 2009; Holland et al. 2014; Fer et al. 2016). Fig. 1b shows the mean tidal current speed, highlighting the enhanced tidal current in the Weddell Sea and the Ross Sea, and over the continental shelf break (close to the 1000 m depth contour). There have been many investigations of the mean along-slope circulation generated by non-linear interaction between tides and sloping bathymetry (e.g., Robinson 1981; Loder 1980; Garreau and Maze 1992), implying that the tidally induced along-slope current increases with stronger stratification (Chen and Beardsley 1995; Brink 2011) and steeper bottom bathymetry (Loder 1980; Kowalik and Proshutinsky 1995; Brink 2010). Huthnance (1973) suggests that the combination of continuity and the Coriolis effects accumulates along-slope momentum, developing residual along-slope current. The bottom drag associated with this residual along-slope current balances the momentum input from tides. Using the vorticity approach, Robinson (1981) shows that tidal oscillations advect positive and negative vorticity to opposite directions, generating residual along-slope circulation. Other previous studies such as Garreau and Maze (1992) also show that the nonlinear dynamics associated with the fluctuating flow act to redistribute momentum in an inviscid ocean. Increasing evidence shows that tidal rectification may be critical to driving the ASC (Flexas et al. 2015; Stewart et al. 2019), reproducing the cross-slope structure and time variability of ASF/ASC. Stewart et al. (2019) have highlighted the interaction between tidal flows and sea ice cover for the circulation and overturning of the ASC. They found that the westward ice-ocean stress vanishes or is even directed eastward in the core of the ASC, possibly due to the acceleration of the ASC by strong tidal momentum advection. These studies imply that models without tides are not likely to correctly represent the geometry, state, or the momentum balance of the ASC.

There have been studies of the interactions between the ASC and sea ice melt/formation (Nicholls et al. 2009; Bull et al. 2021), but the circulation of sea ice within the ASC and the role of sea ice in the ASC momentum budget have received little attention previously. Fig. 1c shows the measured winter climatology of zonal sea ice drift speed. Sea ice drifts westward in most of the ASC, which is in consistent with the direction of the zonal wind (Fig. 1a). In most sectors Antarctic sea ice drift is largely controlled by local wind forcing (Holland and Kwok 2012; Barth et al. 2015). However, close to the coastline or in regions with convergent sea ice motion, where ice internal stresses are large, the correlation between wind and sea ice motion is very low (Holland and Kwok 2012). This suggests that the sea ice drift in the ASC may be affected by other processes, such as tides and buoyancy gradients in the ocean. Note that weak wind/drift correlations may also be expected in regions with nearly static sea ice. Previous studies indicate that the buoyancy gradient in the ocean may play a role in Antarctic sea ice expansion (e.g., Bintanja et al. 2013). However, how buoyancy gradients directly affect the circulation and momentum balance of the sea ice remains unknown. As the ASC is covered by sea ice throughout most of the year, sea ice can modulate the momentum transfer between the atmosphere and the surface ocean when the ASC lies beneath sea ice (Thompson et al. 2018). The surface momentum transfer is traditionally parameterized using the quadratic drag laws. Recent studies indicate that the parameterization depends on ice morphology (Lüpkes et al. 2012) and edge-related turbulence (Lüpkes and Gryanik 2015), and the magnitude of momentum transfer in model simulations differs depending on the choices of surface stress formulation (e.g., Le Paih et al. 2020).

Though there have been numerous studies of how the ASC is driven by winds, eddies, tides, and buoyancy gradients, these studies have largely considered the circulations of the ocean and sea ice independently. It remains poorly understood how the strength and structure of the coupled ocean and sea ice ASC circulation is established by its various drivers. In this study we explore the momentum transfer in the wind-sea ice-ASC system by a suite of experiments with a three-dimensional (3D) high-resolution process-oriented model. In Section 2, we introduce the 3D model configuration, experimental parameters and model evaluation. In Section 3, we use a suite of experiments to identify key controls on the along-slope ice/ocean circulation and transport. The surface ocean and sea ice speeds coincide in the core of the ASC across almost the entire range of experimental parameters, so in Section 4 we investigate this phenomenon using the momentum balance. We show that in the core of the ASC, sea ice horizontally redistributes momentum to the continental shelf and open ocean, while downward eddy momentum transfer is suppressed. In Section 5 we construct a reduced-order model of the ASC to isolate and identify the contributions of tides and eddies to the momentum balance and the ocean/sea ice circulation. Finally, we summarize the results and discuss the caveats and the implications in section 6.

2. Model configuration

In this section we describe the process-oriented model, including the choices that we made to configure the model, the rationale for parameter selection and the model evaluation. Thompson et al. (2018) have identified three major ASC regimes with different circulation and frontal structures: (a) fresh shelf and (b) dense shelf based on whether there is water denser than $\gamma^n = 28.0$ kg/m^3 on the shelf, and (c) warm shelf where ocean temperature at the seafloor of the continental shelf is 2–3°C warmer than the freezing temperature. Either "fresh shelf" or "dense shelf" has cold shelf water, and γ^n is the neutral density. In this study we focus on the "fresh shelf" and "dense shelf" regimes and

use "fresh shelf" as a the reference case to explore parameter dependencies, because fresh shelf occupies the largest fraction of the continental shelf break around Antarctica. In only one experiment with no easterly winds, we touch upon a "warm shelf"-like regime with warm deep water intrusion onto the shelf, though the southernmost of the shelf is restored to the freezing temperature. We use winter-like sea ice conditions for all the simulations because these conditions are representative of more than 8 months of the year (excluding summer and early autumn in Antarctica) in most of the ASC (Holland 2014; Stewart et al. 2019).

This model is developed based on the Massachusetts Institute of Technology General Circulation Model (hereafter the MITgcm, Marshall et al. 1997a,b). We configure the ocean component of this model with the hydrostatic Boussinesq equations and high-order polynomials for the equation of state (McDougall et al. 2003). The sea ice component of this model includes ridging, formation of frazil ice and leads, and has been described in detail by Losch et al. (2010). The sea ice dynamics and thermodynamics are based on Hibler (1979, 1980) and Winton (2000). We choose viscous-plastic ice rheology (Hibler 1979), the Line Successive Relaxation (LSR) sea ice solver (Losch et al. 2014) and seven thickness categories for ice thermodynamics.

Fig. 2 summarizes the configuration of this process-oriented model, and the key parameters used in the simulations are listed in Table 1. The MITgcm has been configured into a 450 km (across-slope, meridional) by 400 km (along-slope, zonal) by 4000 m (depth) domain with horizontal grid spacing of 1 km. As revealed by previous modelling studies (e.g., St-Laurent et al. 2013; Stewart and Thompson 2015), high horizontal resolution (in the order of 1 km) is required to resolve mesoscale eddies over the continental shelf and slope. The vertical grid of the ocean is comprised of 70 geopotential levels with spacing ranging from 10 m at the surface to 100 m at the seafloor. The model has a re-entrant channel in the along-slope direction, with open boundary conditions applied to the onshore (southern) and offshore (northern) boundaries, which is needed to impose tidal flows with realistic amplitudes in this relatively small model domain. The horizontal dimensions of this domain ensure that the mesoscale eddies generated at the open boundaries and re-entering from the other side of the domain do not have a large impact on the slope current, while limiting the computational cost. Previous studies using eddy-resolving process models of the ASC such as Stewart and Thompson (2015, 2016) have used a comparable domain. We add four 50 km-wide troughs to the hyperbolic tangent-shaped bathymetry (Fig. 2a) based on the fact that the Antarctic continental shelf and slope are punctuated by canyons, and that their presence allows topographic form stress to serve as a sink of momentum at the seafloor (Bai et al. 2021). Without submarine troughs, the large wind-input momentum on the shelf must be balanced by bottom frictional stress, which requires an unrealistically large bottom drag coefficient (Stewart and Thompson 2016). The depth and width of the troughs are selected based on observations (e.g., NOAA National Geophysical Data Center 2009), and the reference slope steepness is typical of the Antarctic continental slopes (NOAA National Geophysical Data Center 2009; Amante and Eakins 2009). The full formulation of the model bathymetry is given in Appendix C.

Param.	Value	Description
L_x	400 km	Zonal domain size
L_y	450 km	Meridional domain size
H	4000 m	Maximum ocean depth
H_{shelf}	500 m	Continental shelf depth
Y_s	150 km	Meridional slope position
Z_s	2250 m	Vertical slope position
H_{trough}	300 m	Depth of the troughs
W_{trough}	50 km	Width of the troughs
Y_{trough}	0 km	Southern edge of the trough
L_r	20 km	Thickness of sponge layers
T_{o}^{in}	10 days	Inner relaxation timescale for ocean
$T_{\text{o}}^{\text{out}}$	43200 s	Outer relaxation timescale for ocean
T_{i}^{in}	86400 s	Inner relaxation timescale for sea ice
$T_{\text{i}}^{\text{out}}$	7200 s	Outer relaxation timescale for sea ice
T_{tide}	43200 s	Tidal period
f_0	-1.3×10^{-4} s^{-1}	Reference Coriolis parameter
β	1×10^{-11} (ms)$^{-1}$	Rossby parameter
T_{south}	-1.87°C	Ocean temperature at the southern boundary
C_{ao}	1×10^{-3}	Air-ocean drag coefficient
C_{ai}	2×10^{-3}	Air-ice drag coefficient
C_{io}	5.54×10^{-3}	Ice-ocean drag coefficient
C_{d}	2×10^{-3}	Quadratic bottom-drag coefficient
A_{i}	1	Sea ice concentration
S_{i}	6 psu	Sea ice salinity
ϕ_{fr}	0.3	Salinity retention fraction on freezing
ϕ_{fi}	0.01	Frazil to sea ice conversion rate
T_{a}	-10°C	Surface (2m) air temperature
Q_{a}	5.7 g kg^{-1}	Surface (2m) specific humidity
F_{w0}	324 Wm^{-2}	Reference downward longwave radiation
A_v	3×10^{-4} m^{2}s^{-1}	Vertical eddy viscosity
$A_{4\text{grid}}$	0.1	Grid dependent biharmonic viscosity
κ_v	1×10^{-5} m^{2}s^{-1}	Vertical diffusivity
$\kappa_{4\text{grid}}$	0.1	Grid dependent biharmonic diffusivity
Δ_x, Δ_y	1 km	Horizontal grid spacing
Δ_z	10.5-103.8 m	Vertical grid spacing
Δ_t	80-100 s	Time step

Table 1. List of parameters used in the experiments.

In our experimental configuration we aim to approximately control the sea ice thickness, which is set by an inflow at the southern boundary, while permitting the sea ice to evolve freely in response to mechanical interactions with the atmosphere and ocean. To achieve this, we force

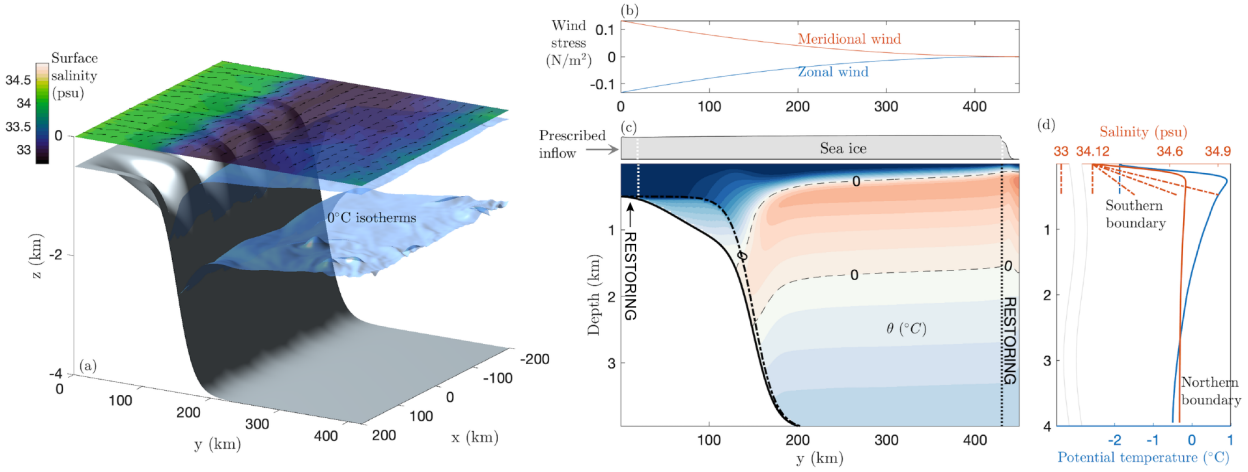

Figure 2. Illustration of the MITgcm Antarctic Slope Front process model (MITgcm_ASF) setup. (a) Model bathymetry, snapshot of sea surface salinity (colors), surface ocean currents (arrows), and 0°C isotherms. (b) The steady along- and across-slope wind forcing used in the reference simulation. (c) Time- and zonal-mean sea ice thickness (the gray box, which is exaggerated) and potential temperature (the contour plot, plotted at intervals of 0.13°C) in the reference simulation. The thick dashed and solid black curves show the shallowest and deepest of the bathymetric contours, respectively. At the southern and northern boundaries, temperature and salinity are restored to the reference profiles across sponge layers of 20 km width. (d) The relaxation salinity (orange) and temperature (blue) profiles of the sponge layers. The northern boundary restoring (solid lines) is based on hydrography taken from the sections across the Antarctic Slope Front at Kapp Norvegia (Hattermann 2018). The southern boundary restoring temperature and salinity are denoted by the dashed lines.

the model at the surface using a fixed atmospheric state, with air-ice momentum and thermodynamic fluxes computed via standard bulk formulae. The magnitudes of the zonal and meridional wind speeds decrease linearly offshore (northward, Fig. 2b), which is consistent with observations (Fig. 1a, also Hazel and Stewart 2019). The remaining atmospheric properties are configured in such a way as to minimize the net air-ice thermodynamic fluxes, and thereby preserve a relatively uniform, winter-like sea ice cover. Specifically, the downward shortwave radiation is set zero to simulate winter conditions, and precipitation is set to zero for simplicity. The surface 2m air temperature (-10°C), humidity (5.7 g kg^{-1}), and downward longwave radiative forcing are horizontally uniform. Note that the air temperature and ice surface temperature (described below) are warmer than typical winter conditions, but they have little impact on the results because the sea ice concentration is approximately 100% in all simulations performed in this study, so our results should be insensitive to such choices as long as the net air-ice energy flux remains close to zero. In our simulations, sea ice surface temperature is warmer than the saltwater freezing temperature and doesn't change much in different simulations. Thinner sea ice loses more heat to the ocean via downward conductive heat flux, because the strength of heat conduction is inversely proportional to ice thickness. Therefore, we prescribe a slightly larger downward longwave radiative forcing ($F_{\rm lw}^{\rm down}$) in experiments with thinner imposed sea ice to ensure that the sea ice thickness won't change much due to thermodynamic processes. We increase $F_{\rm lw}^{\rm down}$ from 324 to 341 Wm^{-2} when the imposed ice thickness decreases from 1 to 0.2 m.

The tidal signal propagates westward around Antarctica as coastal-trapped waves (e.g., Brink 1991). The associated rise and fall of sea surface elevation induces cross-slope barotropic tidal currents. As the coastal-trapped waves are typically much longer than our model domain (e.g., Mysak 1980), tidal flows are generated via imposing a barotropic tidal current on the normal flow through the open northern and southern boundaries, which flow back and forth across the slope. The prescribed tidal currents at the boundaries are (Loder 1980; Brink 2011, 2013)

$$v_t \equiv A_{\rm tide}\ \sin(\omega t),\ \text{at } y = L_y, \tag{1a}$$

$$v_t \equiv A_{\rm tide}\ \frac{H}{H_{\rm shelf}} \sin(\omega t),\ \text{at } y = 0, \tag{1b}$$

where $\omega = 2\pi/43200$s is the tidal frequency, $L_y = 450$ km is the meridional domain size, $H = 4000$ m is the ocean depth at the northern boundary, and $H_{\rm shelf} = 500$ m is the depth of the continental shelf at the southern boundary. The tidal period is set to 12 hours for simplicity, which is close to the period of the dominant tidal constituent (M_2 tide) in most locations. Brink (2011) has found that larger tidal frequency is associated with weaker along-slope rectified flow. Changing tidal frequency also has an impact on the generation of internal tides and mixing (Lamb 2014), which is not investigated in this study since we do not focus on overturning circulation and water mass formation. The tidal amplitude $A_{\rm tide}$ is selected empirically to produce tidal

current speeds comparable to those found around Antarctic margins (Padman et al. 2002, also Fig. 1b). In the reference case, $A_{\mathrm{tide}} = 0.05$ m/s at the northern boundary, so the corresponding barotropic tidal current amplitude is 0.4 m/s at the southern boundary (Fig. 2).

We use two 20-km-width sponge layers at the southern and northern boundaries to relax ice and ocean velocities, potential temperature, salinity, sea ice thickness and ice concentration towards the boundary values. The sponge layers impose a cross-slope buoyancy gradient, which is one of the control parameters in our simulations. The relaxation timescales decrease linearly with distance from the interior termination of the sponge layers towards the outermost boundaries. The relaxation timescales at the innermost and outermost points of the sponge layers are listed in Table 1.

The sea ice concentration near the coastline of East Antarctica is close to 100% in winter (Zwally et al. 2002; Zhang and Rothrock 2003; Stewart et al. 2019) and the thickness is around 1 m (Worby et al. 2008; Zhang and Rothrock 2003), so in the reference case we set the southern boundary sea ice thickness and concentration to 1 m, and 100%, respectively. We prescribe inflow of sea ice through the southern boundary based on the free-drift assumption, because this is the simplest possible choice. Under this assumption, the Coriolis force felt by the sea ice balances the air-ice stress and the ice-ocean stress, so we can solve for the sea ice velocities (U_{i0} and V_{i0}) for given wind speeds (U_{a0} and V_{a0}) at the southern boundary:

$$-\rho_{\mathrm{i}} H_{\mathrm{i0}} f_0 V_{\mathrm{i0}} = \rho_{\mathrm{a}} C_{\mathrm{ai}} \sqrt{U_{\mathrm{a0}}^2 + V_{\mathrm{a0}}^2}\, U_{\mathrm{a0}} - \rho_{\mathrm{o}} C_{\mathrm{io}} \sqrt{U_{\mathrm{i0}}^2 + V_{\mathrm{i0}}^2}\, U_{\mathrm{i0}}, \tag{2a}$$

$$\rho_{\mathrm{i}} H_{\mathrm{i0}} f_0 U_{\mathrm{i0}} = \rho_{\mathrm{a}} C_{\mathrm{ai}} \sqrt{U_{\mathrm{a0}}^2 + V_{\mathrm{a0}}^2}\, V_{\mathrm{a0}} - \rho_{\mathrm{o}} C_{\mathrm{io}} \sqrt{U_{\mathrm{i0}}^2 + V_{\mathrm{i0}}^2}\, V_{\mathrm{i0}}, \tag{2b}$$

The descriptions and values of the parameters in Eq. 2 are listed in Table 1 and Table 2. At the southern boundary, we fix the sea ice velocities to U_{i0} and V_{i0} based on the solutions with different wind speeds and sea ice thickness. Given sea ice thickness at the southern boundary $H_{\mathrm{i0}} = 1$ m, for the reference wind speed $U_{\mathrm{a0}} = -6$ m/s and $V_{\mathrm{a0}} = 6$ m/s, the solutions are $U_{\mathrm{i0}} = -0.14$ m/s and $V_{\mathrm{i0}} = 0.11$ m/s. We impose both zonal and meridional winds instead of imposing zonal wind only because this is more relevant to observations (e.g., Fig. 1 of Hazel and Stewart 2019). In addition, if there is no northward meridional wind and thus no northward sea ice inflow, sea ice would drift southward and pile up at the southern boundary due to the Ekman transport associated with the westward zonal wind, resulting in no sea ice cover over the slope and deep ocean. In this case, the slope current would be too strong because of the strong air-ocean stress; deep convection would occur because the ocean surface is directly exposed to the cold atmosphere. Therefore, we impose meridional wind and northward sea ice drift speed associated with the winds to help maintain sea ice cover over the entire domain.

Initially the sea ice and the ocean are stationary, with ocean temperature and salinity in the interior equal the restoring values at the northern boundary. To reduce computational cost, we start each simulation with a 10-year integration at low resolution (2 km horizontal grid spacing and 30 vertical levels) until it has reached a steady state, then initialize the high-resolution simulations from the corresponding low-resolution simulations. Each high-resolution simulation (1 km horizontal grid spacing and 70 vertical levels) is run for a further 10 years, with a 5-year spin-up and a 5-year analysis period.

Seven model parameters are varied: tidal current amplitude, zonal and horizontal wind speeds, southern boundary sea ice thickness, offshore buoyancy gradient, slope width, and horizontal grid spacing. We independently vary each parameter about the reference values (Table 2), and select the range of the parameters based on typical values in the observations. We use $\Delta\sigma_4$, which is the ocean bottom potential density difference between the northern and the southern boundaries with a reference pressure of 4000 dbar, to quantify the offshore buoyancy gradient. Hence the cases with positive $\Delta\sigma_4$ permit bottom water formation. The cases with relatively fresh continental shelves have vertically uniform salinity profiles at the southern boundary (Fig. 2d), varying from 33.00 to 34.12 psu ($\Delta\sigma_4$ changes from -1.076 to -0.207 kg m^{-3} in Table 2). In the cases named $\Delta\sigma_4 = 0,\ 0.204,\ 0.409$ kg m^{-3}, the salinity equals 34.17 psu at the sea surface at the southern boundary, and increases linearly with depth (Fig. 2d). We need to improve the LSR solver accuracy and increase the number of LSR iterations for the very dense shelf case ($\Delta\sigma_4 = 0.409$ kg m^{-3}) to avoid large imbalance in the sea ice momentum budget over the continental shelf. For all simulations considered in this study, the relaxation temperature at the southern boundary is the freezing temperature (Fig. 2d, Table 1).

We evaluate the model by comparing a cross section of ice and ocean properties in the reference simulation with the hydrography taken in East Antarctica (Fig. 3) during the "BROKE West" survey (Rosenberg and Gorton 2019). We use a summer measurement to evaluate the model because the winter observations are sparse. Some quantitative differences are expected due to the use of summer observations. In general, this idealized reference simulation captures the key features of hydrography and slope current observed in the East Antarctica, with isopycnals incropping at the surface of the continental slope and a westward slope current. Note that the simulation does not aim to closely match the observations, because the bathymetry, boundary conditions, surface forcing and tidal forcing are idealized. Since the hydrography was taken in the Antarctic summer, a thin layer of surface warm water,

Param.	Value	Description
A_{tide}	0, 0.025, **0.05**, 0.075, 0.1 m s^{-1}	Tidal current amplitude at the northern boundary
U_{a0}	-8 **−6**, -4, 0 m s^{-1}	Eastward wind speed at the southern boundary
V_{a0}	4, **6**, 8, 12 m s^{-1}	Northward wind speed at the southern boundary
h_{i0}	0.2, 0.6, **1.0**, 1.4, 1.8, 2.2 m	Sea ice thickness at the southern boundary
$\Delta\sigma_4$	-1.076, -0.620, **−0.207**, 0, 0.204, 0.409 kg m^{-3}	Ocean bottom potential density difference between the northern and the southern boundaries, with a reference pressure of 4000 dbar
W_s	**50**, 100, 150, 200, 250 km	Continental slope width
Δ_x, Δ_y	**1**, 2, 5, 10 km	Horizontal grid spacing

Table 2. List of parameters varied among the experiments. The bold fonts denote the values used in the reference simulation. When varying continental slope width W_s, the corresponding meridional slope position Y_s is **150**, 175, 200, 225, and 250 km, respectively. Note that varying $\Delta\sigma_4$ is achieved by varying the restoring salinity profiles at the southern boundary. In those simulations, the salinity difference between the northern and the southern boundaries at depth z = 500 m are -1.695, -1.108, **−0.578**, -0.315, -0.053, 0.210 psu, respectively (Fig. 2d).

and a layer of relatively colder Winter Water underneath are observed (Fig. 3g). Compared with the observations, the reference simulation has a colder and fresher southern boundary, thus a larger offshore buoyancy gradient near the continental slope (Fig. 3d, e). The isopycnals connecting to the continental slope are steeper in the model which gives rise to a stronger subsurface-intensified along-slope current (Fig. 3f). The model reproduces the key finding of Stewart et al. (2019) with ocean surface velocity approximately matching that of the sea ice (Fig. 3c) over the slope, implying that the sea ice and ocean circulations are tightly linked at the core of the ASC. Note that all the conclusions drawn in this study are based on 100% sea ice cover.

3. Drivers of ASC ocean and sea ice circulation

In section 2 we described the selection of experimental parameters and the ice/ocean circulation in the reference simulation. Now we explore what controls the intensity and structure of the ASC, and quantify the sensitivity of the along-slope ice/ocean circulation and transport to all experimental parameters.

The mean zonal ice and ocean velocities over the continental slope are presented in Fig. 4 and 5. These results agree with previous studies showing that the strength of the ASC increases with stronger zonal wind stress (Fig. 4m-n) and stronger tides (Fig. 4i-j), since they are the principal sources of the westward momentum put into the ice-ocean system (e.g., Thompson et al. 2018; Stewart et al. 2019). The intensification of the ASC with tides agrees with previous studies on tidal rectification (e.g., Huthnance 1973; Robinson 1981). The intensity of zonal ocean and sea ice velocities changes dramatically with ice thickness (Fig. 4e, l), because the resistance of sea ice chunks to deformation caused by external forcing decreases with reduced ice thickness (Hibler 1979). When the sea ice is thin enough ($h_{\text{i0}} \lesssim 0.2$ m), the resistance to deformation is sufficiently weak that a strong ice jet forms over the continental slope (Fig. 4e). Our results also show that the intensity of slope current increases with steeper topographic slope, the reason for which will be discussed in section 4.

The structure of the slope current changes dramatically with offshore buoyancy gradient, shifting from a surface-intensified flow, to a barotropic structure, and to a bottom-intensified flow as salinity increases at the southern boundary (Fig. 5g-l). This structural change is supported by observational evidence from the Weddell Sea (Le Paih et al. 2020). In the cases with reference restoring salinity, the shelf water below the surface is less dense than the water offshore ($\Delta\sigma_4 = -0.207$ kg m^{-3}). Thus the isopycnals in the deep ocean tilt down to the south and incrop on the continental slope (Fig. 5i), which gives rise to a slope current that is intensified with elevation above the bathymetry, via the thermal wind relation. When the shelf is very fresh ($\Delta\sigma_4 = -1.076$ kg m^{-3}), the shape of the interior density front generates strong vertical velocity shear. The westward velocity weakens with ocean depth, and reverses to the east, causing an undercurrent (opposite the wind direction) over the slope (Fig. 5g). When there is bottom water formation ($\Delta\sigma_4 = 0.204,\ 0.409$ kg m^{-3}), the westward slope current is bottom-intensified, with an eastward undercurrent above (Fig. 5k-l), because the offshore dense outflow and the onshore return flow are deflected by the Coriolis force.

To quantify the sensitivity of the along-slope circulation to various parameters, we calculate the following quantities over the continental slope: the maximum westward velocity throughout the water column ($|\overline{u_{\text{o}}}|_{\max}$) and at the seafloor ($\left|\overline{u_{\text{o}}^{\text{bot}}}\right|_{\max}$), the barotropic and baroclinic transports (T_{BT}, T_{BC}), the westward sea ice velocity ($|\langle\overline{u_{\text{i}}}\rangle|$) and the sea ice thickness ($\langle\overline{h_{\text{i}}}\rangle$). Here the overlines denote an average over a 5-year analysis period,

$$\overline{\bullet} = \frac{1}{5\text{ years}} \int_{t_0}^{t_0+5\text{ years}} \bullet \, dt, \tag{3}$$

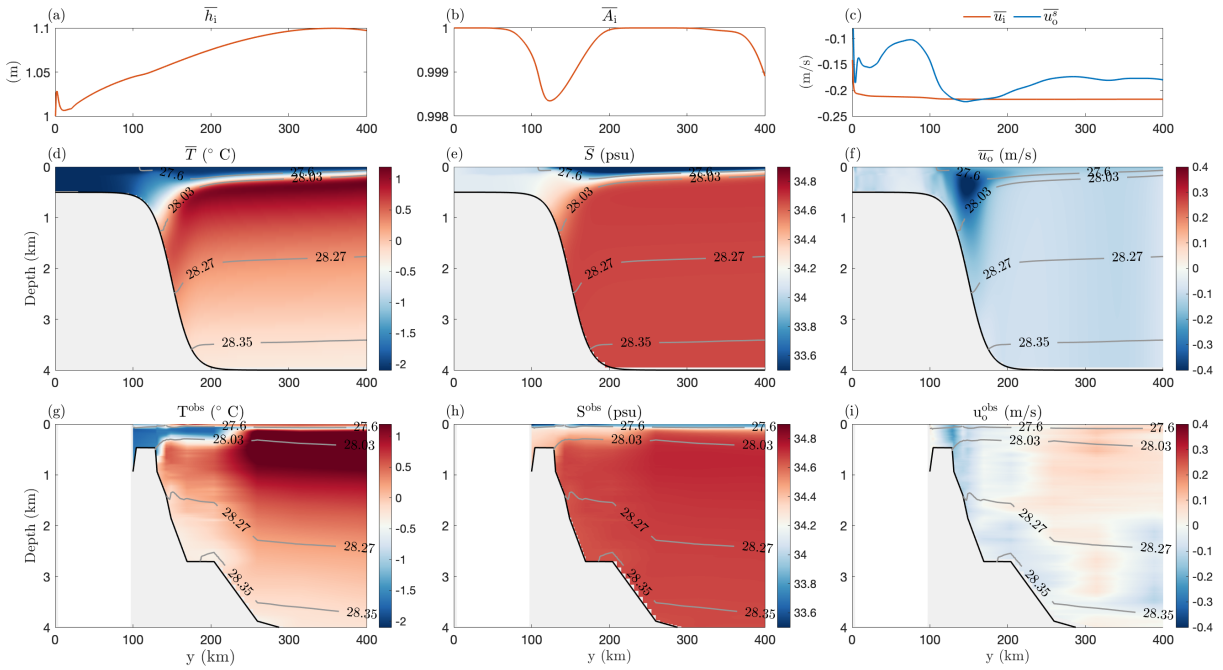

Figure 3. Model evaluation. (a-f) A cross section of ice and ocean properties in the reference simulation using time-mean output, taken along the longitude $x = 0$ km. (g-i) The hydrography taken near East Antarctica during the "BROKE West" survey (Rosenberg and Gorton 2019) in the Antarctic summer of 2006, along the 60°E line. (a) Sea ice thickness. (b) Sea ice concentration. (c) Sea ice and surface ocean zonal velocities. (d, g) Ocean potential temperature. (e, h) Ocean salinity. (f, i) Ocean zonal velocity. The values on the gray contours denote the neutral densities (kg/m^3).

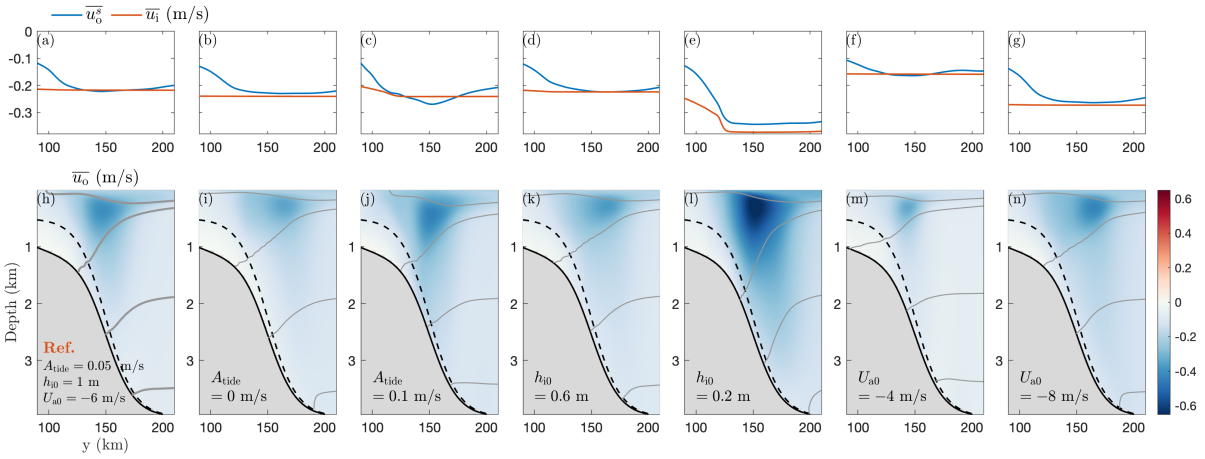

Figure 4. Time- and zonal-mean zonal velocity for the reference simulation (a, h), simulations with varying tidal current amplitudes (b, c, i, j), thinner sea ice at the southern boundary (d, e, k, l), and varying zonal wind speeds (f, g, m, n). The corresponding upper panels show the time- and zonal-mean zonal ice and surface ocean velocities. The gray contours denote the time- and zonal-mean neutral densities 1027.60, 1028.03, 1028.27, and 1028.35 kg/m^3. Dashed and solid thick black curves denote the shallowest and deepest of the bathymetric contours, respectively. In these simulations, the southern boundary temperature and salinity are set to be vertically uniform (-1.87 °C, 34.17 psu).

and the angle brackets $\langle \bullet \rangle$ denote an average over the continental slope,

$$\langle \bullet \rangle = \frac{1}{L_x W_s} \oint dx \int_{L_0}^{L_0+W_s} \bullet \, dy, \qquad (4)$$

where $L_x = 400$ km is the zonal domain size, W_s is the width of the continental slope, and $L_0 = 125$ km is the starting point of the slope in the meridional direction. The continental slope is defined as the region between the lat-

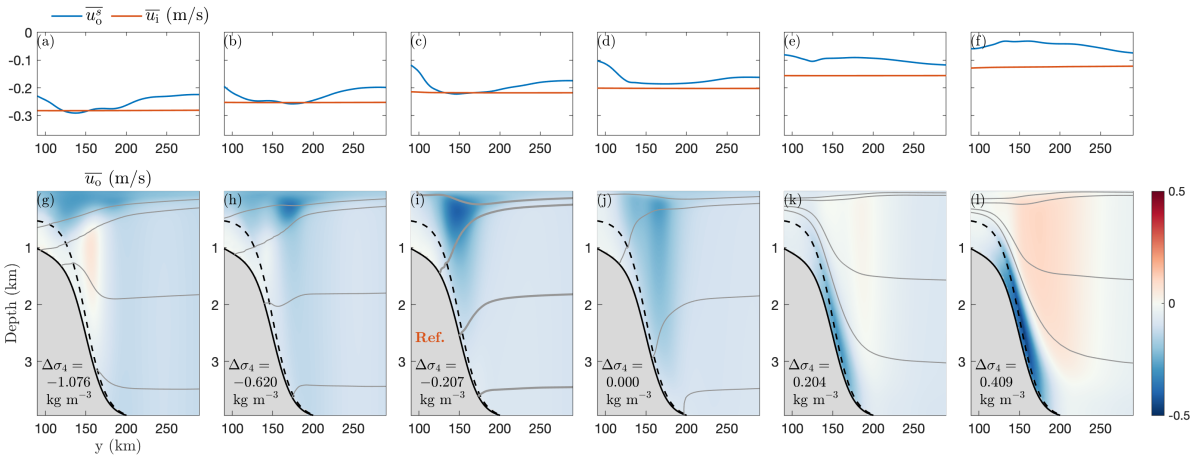

Figure 5. Time- and zonal-mean zonal velocity varying with buoyancy gradients between the continental shelf and the open ocean. Similar to Fig. 4, the corresponding upper panels show the time- and zonal-mean zonal ice and the surface ocean velocities. The gray contours denote the time- and zonal-mean neutral densities and the black curves denote the model bathymetry. Other model parameters such as tidal current amplitude, wind speeds, sea ice thickness at the southern boundary, and slope width are the same in these simulations.

itudes $y = L_0$ and $y = L_0 + W_s$. The total zonal transport per unit length in the ASC (T_{total}) is the vertically integrated time-mean zonal ocean velocity, averaged over the slope. Its barotropic component (T_{BT}) is the time-mean seafloor zonal velocity ($\overline{u_o^{\text{bot}}}$) times the ocean thickness (h), averaged over the slope. The baroclinic component (T_{BC}) is the difference between the total transport and the barotropic transport. T_{total}, T_{BT}, and T_{BC} are defined to be positive westward,

$$T_{\text{total}} = \left\langle -\int_{-h}^{0} \overline{u_o} dz \right\rangle, \quad T_{\text{BT}} = \left\langle -\int_{-h}^{0} \overline{u_o^{\text{bot}}} dz \right\rangle, \quad (5)$$
$$T_{\text{BC}} = T_{\text{total}} - T_{\text{BT}}.$$

We find that the barotropic tides change the barotropic transport, while it does not affect the baroclinic transport (Fig. 6a). Sea ice thickness, wind stress, slope steepness and horizontal resolution mainly affect the baroclinic transport (Fig. 6b-f). Fig. 6g highlights the changes in the barotropic and baroclinic transport due to increased offshore buoyancy gradient, which is in agreement with Fig. 5. As for the circulation of the sea ice, Fig. 7 shows that the trends of $|\langle \overline{u_i} \rangle|$ is approximately consistent with the total transport of the ocean, whereas $|\langle \overline{u_i} \rangle|$ is less sensitive to varying slope width. The along-slope sea ice velocity decreases with increased offshore buoyancy gradient (Fig. 7b), as it is accelerated by the surface-intensified ocean current in fresh-shelf case, and is damped by the eastward undercurrent in the dense-shelf case. The sea ice thickness averaged over the slope is mostly controlled by the prescribed ice thickness at the southern boundary, with an exception in the case $V_{a0} = 12$ m/s, where the sea ice piles up in the middle of the domain due to strong offshore advection imposed by the southern inflow boundary condition, and convergence of meridional ice flow associated with the meridional gradient of the meridional wind stress.

In most simulations, the surface ocean velocity approximately matches the velocity of the sea ice over the continental slope, even in the case with no tides, as shown in the upper panels of Fig. 4 and 5. Exceptions include cases with very thin sea ice (Fig. 4e), a dense southern boundary (Fig. 5e-f), and a wide topographic slope (shown later in the next section). To understand the mechanisms that control the ice/ocean circulation, and identify the cause of the ice-ocean velocity match over the slope, we look into the momentum balances of the ice/ocean system in the following section.

4. Momentum balances for ocean and sea ice in the ASC

A simple and intuitive speculation regarding momentum transfer in the wind-sea ice-ocean system is that the wind inputs momentum to the sea ice, and then the sea ice accelerates the ocean by ice-ocean stress. Some previous studies that have worked under this assumption include Nøst et al. (2011), Stewart and Thompson (2016) and Huneke et al. (2019). The momentum is vertically transferred downward through the ocean, primarily via eddy-induced isopycnal form stress, and is finally removed by bottom frictional stress and topographic form stress at the seafloor (Stewart and Thompson 2016; Bai et al. 2021). However, in section 3 we found that over a large range of model parameters, ocean surface velocity matches the velocity of sea ice over the continental slope; while over the shelf and in the deep ocean, ice and ocean velocities diverge. This is consistent with the results of Stewart et al. (2019). This indicates

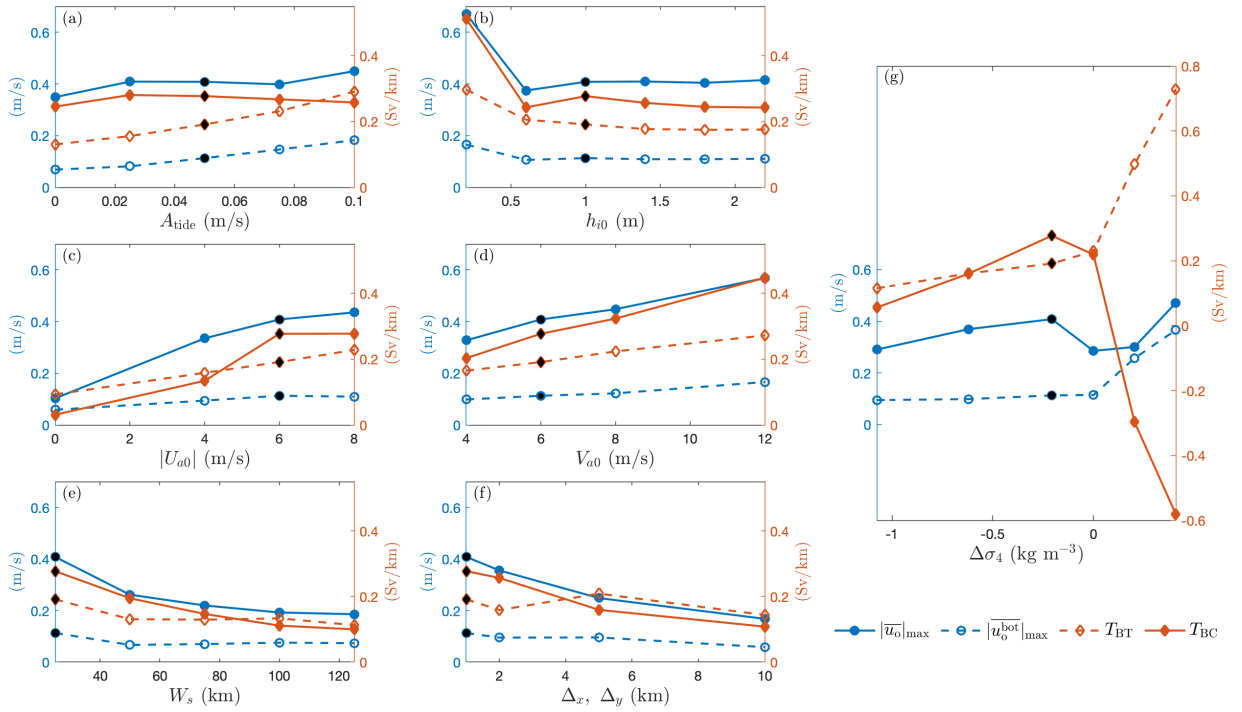

Figure 6. The maximum westward ocean speed $|\overline{u_{\rm o}}|_{\rm max}$, maximum westward ocean bottom speed $\left|\overline{u_{\rm o}^{\rm bot}}\right|_{\rm max}$, barotropic transport $T_{\rm BT}$ and baroclinic transport $T_{\rm BC}$ per unit width over the continental slope for simulations with varying tidal current amplitude (a), sea ice thickness at the southern boundary (b), maximum westward wind speed (c), maximum northward wind speed (d), continental slope half-width (e), horizontal grid spacing (f), and ocean bottom potential density difference between the northern and the southern boundaries (g). Black dots denote the reference simulation.

that some processes occurring over the slope diminish the ice-ocean momentum transfer there, so the speculation discussed above is incomplete. In order to establish the pathways of the wind-input momentum over the slope, and to understand how the wind, sea ice, tidal forcing, offshore buoyancy gradients and bathymetry influence the momentum transfer, we analyze the zonal momentum balances of the ice and ocean system.

a. Zonal momentum balance in the reference simulation

In the spin-up stage, when the ASC transitions from stationary state to equilibrium state, some combination of the winds, tides and bottom stresses (Howard et al. 2015) spins up the flow (not shown) until the speeds of sea ice and surface ocean approximately coincide over the slope. We did not distinguish the relative importance of each in the spin-up stage because in nature the ASC already exists, so the steady-state dynamics are more relevant. In this study we focus on the momentum balance in the equilibrium state, when the slope current continues in its state of motion. The current feels almost no drag against the sea ice, so almost no additional momentum source is needed to maintain its motion (Newton's first law).

The vertically and zonally integrated zonal momentum equations for the ocean and the sea ice solved by MITgcm are

$$\oint \underbrace{\rho_{\rm o}\int_{-h}^{0}\frac{\partial \overline{u_{\rm o}}}{\partial t}dz}_{\text{Tendency}}dx = \oint\Big(\underbrace{\overline{\tau_{\rm io}^{x}}}_{\substack{\text{Ice-ocean}\\ \text{stress}}} \underbrace{-\rho_{\rm o}\int_{-h}^{0}\overline{\boldsymbol{u}_{\rm o}\cdot\boldsymbol{\nabla}\boldsymbol{u}_{\rm o}}\,dz}_{\text{Ocean advection}} \underbrace{+\rho_{\rm o}f\int_{-h}^{0}\overline{v_{\rm o}}\,dz}_{\text{Coriolis}} \underbrace{-\overline{p_b}\frac{\partial \eta_b}{\partial x}}_{\text{Topog. form stress}} \underbrace{-\overline{\tau_b^{x}}}_{\substack{\text{Bottom}\\ \text{frictional stress}}} \underbrace{+\mathcal{V}}_{\substack{\text{Viscous}\\ \text{diffusion}}}\Big)dx, \tag{6a}$$

$$\oint \underbrace{\rho_{\rm i}\overline{h_{\rm i}\frac{\partial u_{\rm i}}{\partial t}}}_{\text{Tendency}}dx = \oint\Big(\underbrace{\overline{\tau_{\rm ai}^{x}}}_{\substack{\text{Wind}\\ \text{stress}}} \underbrace{+\frac{\partial \overline{\sigma_{21}}}{\partial y}}_{\text{Ice rheology}} \underbrace{+\rho_{\rm i}f\overline{h_{\rm i}v_{\rm i}}}_{\text{Coriolis}} \underbrace{-\overline{\tau_{\rm io}^{x}}}_{\substack{\text{Ice-ocean}\\ \text{stress}}}\Big)dx. \tag{6b}$$

Here the subscripts "i" and "o" denote the sea ice and the ocean respectively, p_b is the bottom pressure, and η_b is the seafloor elevation. As the time-averaged mass flux is zero across the northern and the southern boundaries, the Coriolis term is very small in Eq. 6a, though in practice it is non-zero due to the spatial discretization in MITgcm.

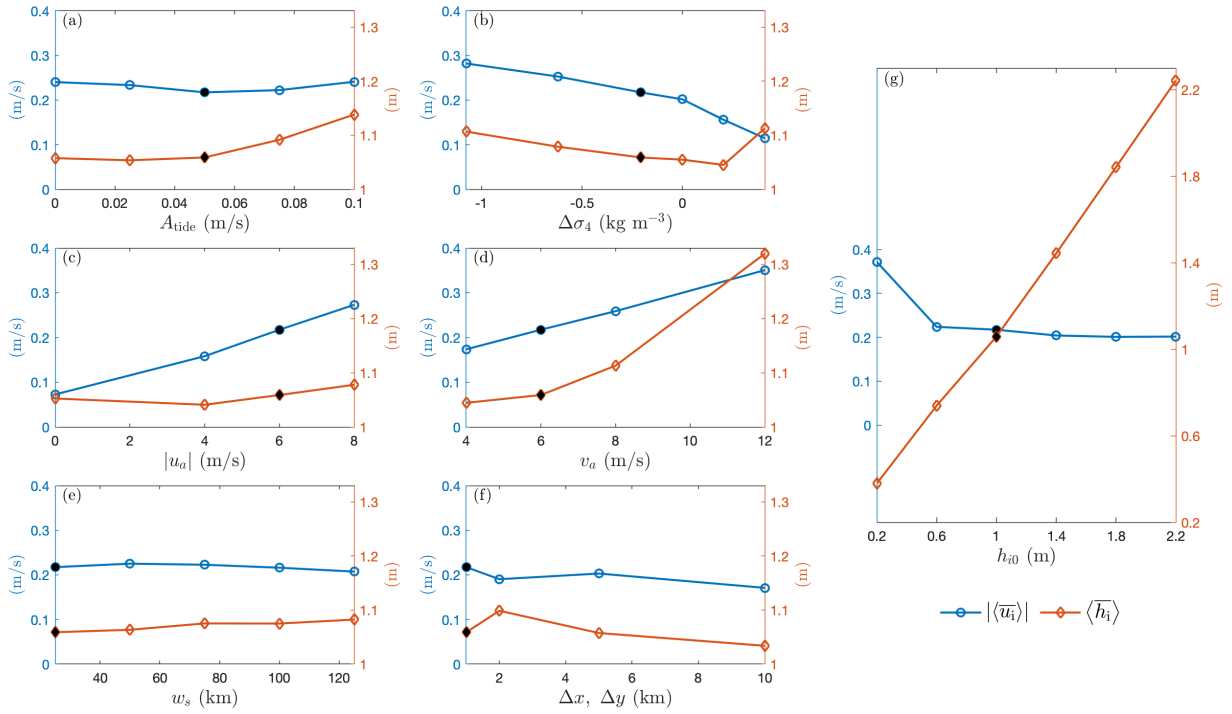

Figure 7. Time-mean westward ice speed $|\langle\overline{u_i}\rangle|$ and ice thickness $\langle\overline{h_i}\rangle$ over the continental slope, for simulations with varying tidal current amplitude (a), ocean bottom potential density difference between the northern and the southern boundaries (b), maximum westward wind speed (c), maximum northward wind speed (d), continental slope half-width (e), horizontal grid spacing (f), and sea ice thickness at the southern boundary (g). Black dots denote the reference simulation.

The symbols with σ and indices in the subscription are components of the sea ice internal stress in the standard form, which quantify the resistance of sea ice to deformation (Hibler 1979). The zonal component of the sea ice internal stress divergence is $\partial_x\sigma_{11}+\partial_y\sigma_{21}$. After taken the zonal integration, $\partial_x\sigma_{11}$ has no contribution to the sea ice momentum budget. The sea surface slope $-\rho_{\rm i}h_{\rm i}g\partial\eta/\partial x$ and ice/snow load $-\rho_{\rm i}h_{\rm i}g\partial(h_{\rm i}\rho_{\rm i}/\rho_{\rm o})/\partial x$ also vanish approximately under a zonal integral. Sea ice momentum advection is negligible and is turned off in MITgcm by default.

Fig. 8a shows the sea ice zonal force balance of the reference simulation. As assumed by previous studies (Nøst et al. 2011; Stewart and Thompson 2016; Huneke et al. 2019), the overall momentum balance of the sea ice is primarily between wind stress and ocean-ice stress. This is largely the case over the continental shelf and the open ocean. However, over the slope there is substantial horizontal redistribution of momentum via ice internal stress divergence, and the ocean-ice stress is almost zero. The green arrows in Fig. 8a show the momentum fluxes due to sea ice internal stress, which indicate that over the slope the sea ice mainly transfers wind-input momentum onto the continental shelf in the reference case. The Coriolis force felt by the sea ice is negative and approximately uniform, because the time-averaged meridional ice velocity is dominated by the northward ice inflow from the southern boundary.

The ocean zonal force balance of the reference simulation is shown in Fig. 8b. For the ocean, the primary momentum input from ice-ocean stress is balanced by topographic form stress (TFS) on the shelf and bottom frictional stress in the open ocean. The secondary momentum input from ocean advection, including the lateral momentum transfer and momentum flux convergence due to tidal rectification, is balanced locally by bottom frictional stress, and thus does not affect the overall picture of the momentum balance. Over the continental shelf, the sea ice flows much faster than the ocean, injecting westward momentum into the ocean via ice-ocean stress. TFS might be expected to be the primary sink of momentum in analogy with the Antarctic Circumpolar Current (ACC, Munk and Palmén 1951; Masich et al. 2015; Stewart and Hogg 2017), but it was unclear previously how important the TFS is in the ASC, since the directions of the ACC and the ASC are opposite relative to topographic Rossby wave propagation (Bai et al. 2021). In this model with bumps and troughs added to the bathymetry (Fig. 2a), TFS is able to extract momentum from the flow on the shelf to balance the momentum input from ice-ocean stress. The inclusion of bumps and troughs is more realistic than the uniform geometries used in previous studies (e.g., Stew-

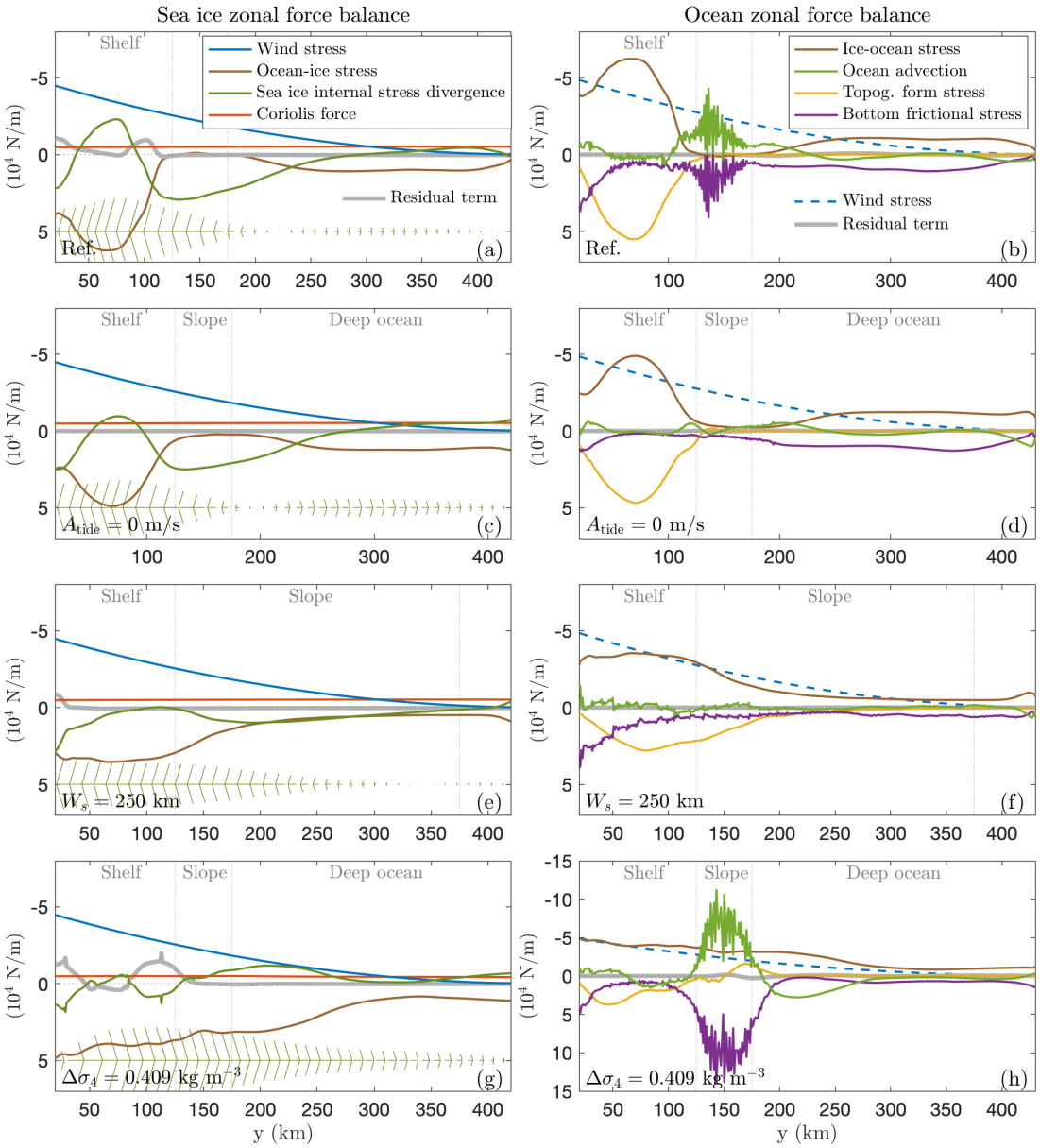

Figure 8. Time- and zonal-mean sea ice and ocean zonal force balances for the reference simulation (a, b), the case with zero tidal current amplitude (c, d), the case with a wide and gentle continental slope (e, f), and the very dense shelf case (g, h). Note that the 20-km southern and northern restoring regions have been removed. The y-axis is negative (westward) upward, and the range of y-axis for panel (h) is different from other panels.

art and Thompson 2016; Huneke et al. 2019; Stern et al. 2015). Excluding the bumps and troughs would lead to stronger flows along the shelf, and we don't anticipate this changing the findings qualitatively.

The presence of strong advective acceleration also deviates from the speculative momentum balance laid out at the beginning of section 4. By temporally decomposing the total ocean advection into mean, eddy, and tidal components, we find that ocean advection is mostly contributed by tidal advection in the reference case (Appendix B), which is strongest over the slope because tidally induced momentum convergence is proportional to topographic slope steepness (Loder 1980). The tide-input momentum (tidal advection) is balanced by bottom drag associated with the along-slope tidally rectified flow (Fig. 8b), which is consistent with previous studies on the mechanisms of tidal rectification (e.g., Huthnance 1973). Additionally, the varying thickness of the staircase-like bottom grid cells generates convergence

and divergence in the bottom Ekman transport (Brink and Lentz 2010), leading to numerical noise in ocean advection and bottom frictional stress (Fig. 8b, h). However, there is no distinguishable noise in the velocity field (Fig. 4-5), and the residual term is zero in the ocean momentum balance (Fig. 8), suggesting that the overall momentum balance is not contaminated by the numerical noise.

b. Sensitivity of zonal momentum balance to model parameters

Across a wide range of experimental parameters, the pattern of the zonal force balance is qualitatively similar to the reference case (Fig. 9), neither very sensitive to wind speed perturbations (Fig. 9c-f) nor sea ice thickness (Fig. 9a-b). As the sea ice strength is proportional to ice thickness, thinner sea ice has less resistance to deformation imposed by external forcing (Hibler 1979), leading to increased ice-ocean shear (Fig. 4e, Fig. 9a) and decreased ice internal stress divergence (Fig. 9a). The results suggest that the characteristics of the momentum balance do not qualitatively depend on meridional gradient in zonal wind stress (Fig. 9c-f). When varying wind speeds, we also change the meridional gradient of the wind, as the magnitude of the wind speeds decrease linearly offshore to zero at the northern boundary. In addition, the direction of sea ice momentum transfer (onto the shelf, in many cases, see Fig. 9) is against the gradient of wind-input momentum.

In a few cases with wider topographic slope (smaller steepness compared with typical slope steepness around Antarctica, Fig. 10c) and dense water outflows (Fig. 10e), sea ice internal stress divergence does not redistribute most of the wind-input momentum over the slope. The magnitude of the ice-ocean stress increases substantially with offshore buoyancy gradient $\Delta\sigma_4$ (Fig. 10f), consistent with Fig. 5l. The strength of ocean bottom velocity increases with $\Delta\sigma_4$ (Fig. 6g), leading to a much larger bottom frictional stress over the slope (Fig. 8h, 10f), which is balanced by enhanced ocean advection and ice-ocean stress. Note that the residual term in the sea ice momentum budget is non-zero in some cases (Fig. 8a, 8g), but our tests indicate that improving the LSR solver accuracy would reduce those errors, with little impact on the momentum balance.

Stewart et al. (2019) indicate that tides are responsible for the match of ocean and sea ice velocities over the continental slope. Our results show that tidal advection indeed accelerates the ocean and decreases ice-ocean stress over the shelf break. However, tides are not required for the ice-ocean stress to vanish over the slope. Fig. 8c and 8d show the sea ice and ocean zonal force balances for a simulation with no tides. In this case, the matching of the ice and surface ocean velocities still occurs. When the tidal current is very strong, the ocean surface velocity exceeds the velocity of sea ice (Fig. 4c), causing ocean-to-sea ice westward momentum transfer (Fig. 10b).

c. Vertical momentum transfer over the slope

Fig. 11c shows the vertical profiles of zonal velocity in cases with varying topographic slope steepness, averaged over each slope. In the reference case, the vertical velocity shear in the ocean interior is large (the black curve in Fig. 11c), suggesting that the vertical momentum transfer is inefficient over the slope. The mesoscale eddies in the ocean transfer momentum downward predominantly by isopycnal form stress (IFS), which is essential to connecting the momentum input from ocean surface, and the momentum sink at seafloor (e.g., Vallis 2017). Fig. 11a-b show the estimated transient and standing eddy vertical momentum fluxes due to IFS and vertical component of Reynolds stress, normalized by wind stress over the slope. In the reference case, in which the slope steepness is typical of the Antarctic continental slope (NOAA National Geophysical Data Center 2009; Amante and Eakins 2009), the transient and standing eddies are not effective in transferring momentum downward. This is consistent with previous studies that report suppression of baroclinic instability over steep slopes (Isachsen 2011; Hetland 2017).

With decreased topographic slope steepness, the standing and transient eddies are more efficient in transferring momentum downward over the slope (11a-b). The resulting ocean velocity shear decreases (11c), and the ocean surface velocity falls substantially below the speed of the sea ice. Thus the ice-ocean velocity shear (11c) and the ice-ocean stress (Fig. 10d) increase with larger slope width. In the case W_s=250 km, the ice-ocean stress approximately matches the wind stress (Fig. 8f).

5. A reduced-order model of ice-ocean mechanical interactions in the ASC

As discussed in section 4, our results suggest that vertical momentum transfer by standing and transient eddies is inefficient over continental slopes steepnesses typical of Antarctica. However, since we can not explicitly turn off eddy suppression in the 3D models, the mechanism responsible for ice-ocean coupling in the core of the ASC, and to what extent topographic eddy suppression affects the momentum budget, remain unclear. To provide insight into the underlying mechanism, we develop a reduced-order model of ice-ocean mechanical interactions, which is primarily a tool to test the relevance of eddy suppression over the slope. In this model, the ocean is discretized into two vertical levels of equal depth, overlaid by one layer of viscous-plastic sea ice and forced by a specified atmospheric wind stress. We incorporate the effect of eddies via a "residual-mean" formulation of the momentum equations, with an eddy isopycnal form stress that transfers momentum vertically between the two layers, with the rate of momentum transfer being controlled by an eddy diffusivity (Ferreira and Marshall 2006). This allows us to optionally suppress vertical eddy momentum transfer over the slope, and thereby

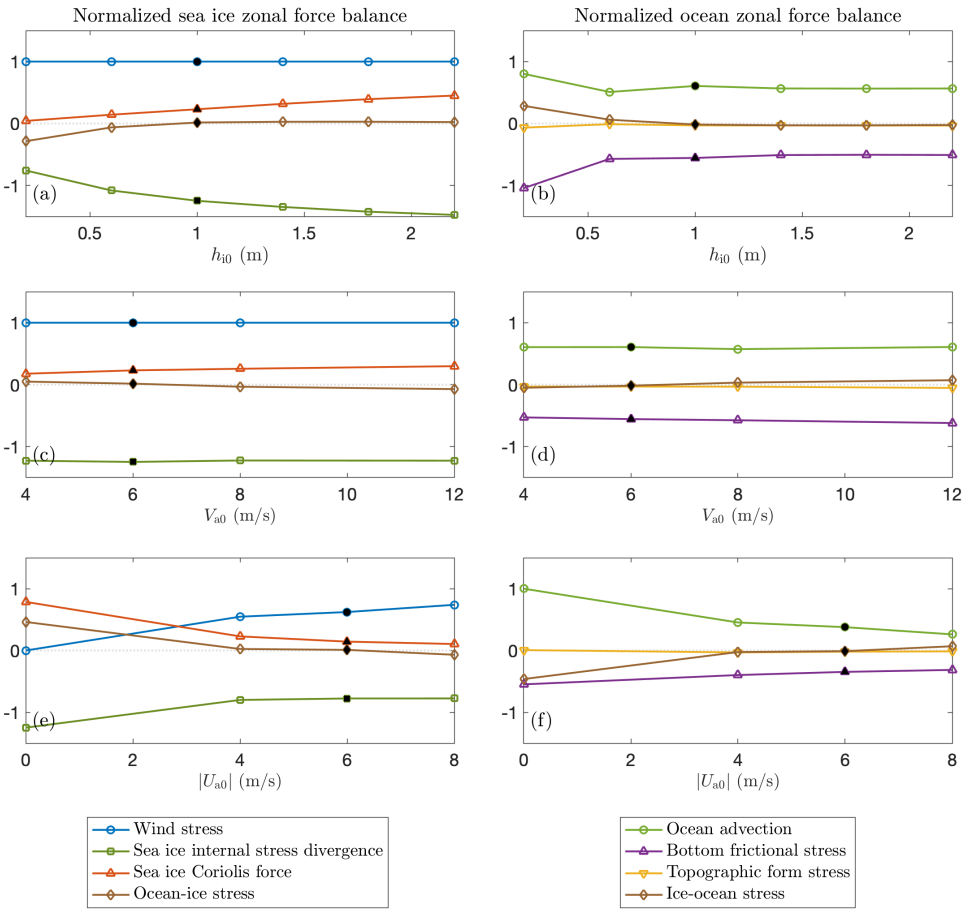

Figure 9. Sensitivity analysis: time-mean sea ice and ocean zonal force balances averaged over the continental slope, (a-d) normalized by zonal wind stress, or (e-f) by the sum of zonal wind stress and ocean advection. Simulations with varying (a-b) sea ice thickness at the southern boundary, (c-d) maximum northward wind speed, and (e-f) maximum westward wind speed.

isolate the role of eddy suppression from other processes that can reduce ice-ocean shear, such as tidal forcing. In this section we describe the reduced-order model configuration, compare cases with and without eddy suppression over the slope, and compare the results of reduced-order simulations with the 3D MITgcm simulations.

a. Formulation of the reduced-order model

To simplify the equation of motion, the flow is assumed to be steady ($\partial_t \equiv 0$), invariant in the x-direction ($\partial_x \equiv 0$), and low-Rossby number ($D/Dt \equiv 0$). We consider cases with a weak horizontal buoyancy gradient only, hence the assumption of zero time-averaged meridional (offshore) flow in the ocean. We apply the Boussinesq momentum equations, and fix the densities of the sea ice (ρ_i = 920 kg/m^3) and the ocean (ρ_o = 1037 kg/m^3).

The upper level of the ocean is driven by ice-ocean stress and transfers momentum downward to the lower level via isopycnal form stress (IFS). For the lower level, the momentum input by IFS and tidal advection sinks at the seafloor via bottom frictional stress and topographic form stress. Though the tidal current imposed at the boundaries are barotropic, the tide-induced momentum flux convergence in the ocean, i.e., tidal advection, is bottom intensified. Bottom frictional stress creates a phase lag between the meridional tidal velocity and the transient zonal velocity induced by tides, which regulates the magnitude of the tidal advection (e.g., Huthnance 1973; Loder 1980). Therefore, we only consider the tidal advection term for the lower level where fiction appears. The momentum equations for the ocean are

$$\underbrace{\rho_o h_o^s \frac{\partial u_o^s}{\partial t}}_{\text{Tendency}} = \underbrace{\tau_{io}^x}_{\substack{\text{Ice-ocean}\\ \text{stress}}} \underbrace{- F_{ifs}}_{\substack{\text{Isopycnal}\\ \text{form stress}}}, \tag{7a}$$

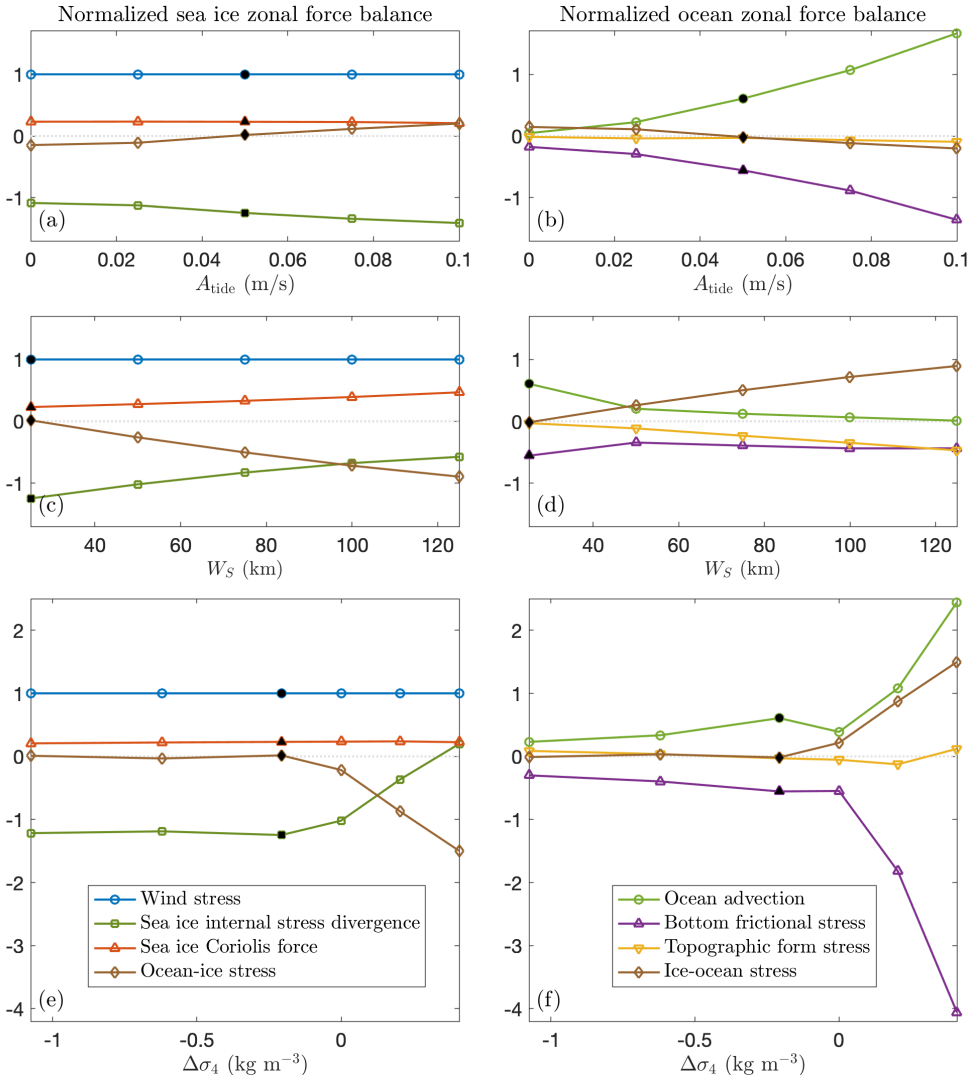

Figure 10. Sensitivity analysis (continued): time-mean sea ice and ocean zonal force balances, averaged over the continental slope and normalized by zonal wind stress. Simulations with varying (a-b) tidal current amplitude, (c-d) continental slope half-width, and (e-f) ocean bottom potential density difference between the northern and the southern boundaries.

$$\underbrace{\rho_o h_o^b \frac{\partial u_o^b}{\partial t}}_{\text{Tendency}} = \underbrace{F_{\text{ifs}}}_{\substack{\text{Isopycnal}\\ \text{form stress}}} \underbrace{+\tau_b^x}_{\substack{\text{Bottom}\\ \text{frictional}\\ \text{stress}}} \underbrace{+F_{\text{tide}}}_{\substack{\text{Tidal}\\ \text{advection}}} \underbrace{+F_{\text{tfs}}}_{\substack{\text{Topographic}\\ \text{form stress}}}, \quad (7b)$$

$$h_o^s = h_o^b = \frac{h_o}{2}, \quad (7c)$$

where the superscripts "s", "b", "x", and "y" denote the upper (surface) and the lower (bottom) levels, and the components in the zonal and the meridional directions, respectively. Note that the interface between the upper and the lower levels should not be interpreted as an isopycnal surface, but rather as a terrain-following coordinate. This formulation can also be derived by considering the evolution of the surface and bottom ocean velocities, and assuming a linear vertical variation between them.

The IFS can be estimated by the product of isopycnal slope and eddy diffusivity (e.g., Vallis 2017). We assume that the ocean is in geostrophic balance, which is equivalent to assuming that eddies release available potential energy and relax isopycnal slopes (Gent and Mcwilliams 1990; Gent et al. 1995). Then we express the isopycnal slope by the thermal wind relation and assume the horizontal variations in the vertical stratification are very weak. Ultimately we relate IFS to vertical velocity shear, so the isopycnal slope and the IFS can evolve dynamically with

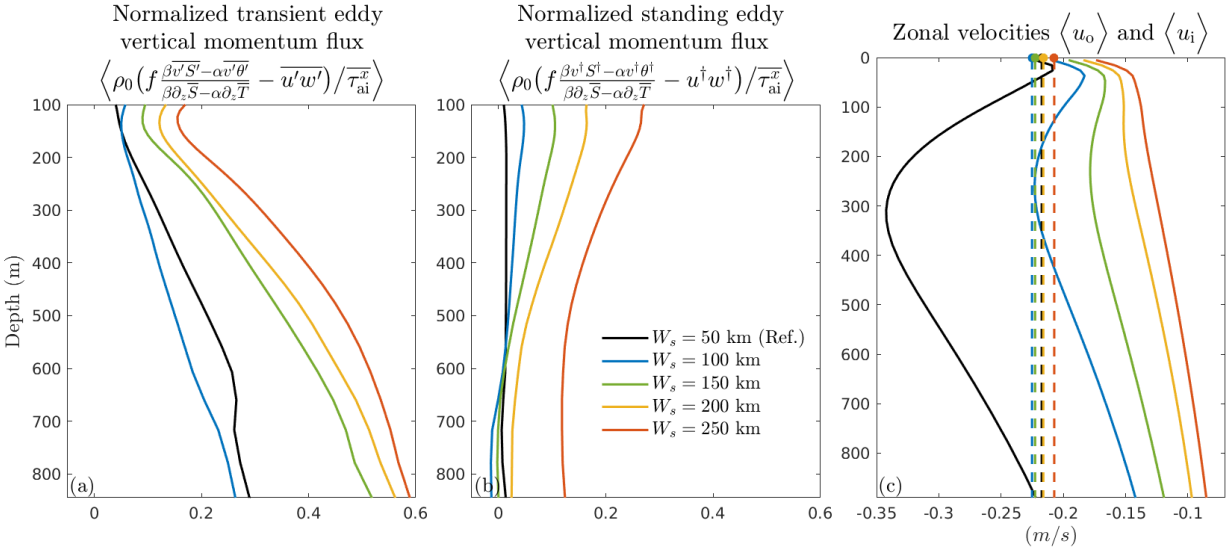

Figure 11. (a) The vertical component of the transient eddy momentum flux for cases with varying slope width, normalized by wind stress. The angle brackets denote the averaged values over the continental slope (Eq. 4). The overbars denote the time average over a 5-year analysis period (Eq. 3), and primes denote departures of state variables from their respective time-averaged values. The first term in the numerator is the estimated isopycnal form stress (IFS) due to transient eddies, and the second term is the vertical component of the Reynolds stress. (b) The vertical component of the standing eddy momentum flux for cases with varying slope width, normalized by wind stress. The daggers denote departures of state variables from their zonally averaged values. The first term in the numerator is the estimated IFS due to standing eddies. (c) Zonal ocean (solid curves) and sea ice (dashed lines) velocities averaged over the continental slope for cases with different slope width. (a)-(c) are plotted from 100 to 800 meters depth to exclude the bottom bathymetry and the surface mixed layer where the ocean is weakly stratified and the estimation of IFS from the density (or equivalently T and S) gradient is invalid.

time. The IFS in the reduced-order model is

$$F_{\text{ifs}} = 2\rho_{\text{o}} f^2 K \frac{(u_{\text{o}}^s - u_{\text{o}}^b)}{N^2 h_{\text{o}}}, \tag{8}$$

where K is the eddy diffusivity, and $N \approx 8.3\times10^{-4}\text{s}^{-1}$ is the mean stratification (buoyancy frequency) between the upper and the lower levels, obtained from the restoring density profile at the northern boundary of the MITgcm simulations (Fig. 2d). Note that this eddy diffusivity parameterization only represents the diffusivity due to transient eddies. Since the vertical eddy momentum flux is mostly contributed by transient eddies for the reference slope steepness (Fig. 11a-b), this model does not include a standing eddy parameterization for simplicity. Details on the derivation of the IFS are in Appendix A2.

The sea ice follows a standard viscous-plastic rheology given by Hibler (1979) (Appendix A6). Assuming that the ocean is fully covered by the sea ice (the ice concentration is $A_{\text{i}} = 1$), the momentum equations for the sea ice are

$$\underbrace{\rho_{\text{i}} h_{\text{i}} \frac{\partial u_{\text{i}}}{\partial t}}_{\text{Tendency}} = \underbrace{\rho_{\text{i}} h_{\text{i}} f v_{\text{i}}}_{\text{Coriolis}} \underbrace{+\tau_{\text{ai}}^x}_{\substack{\text{Wind}\\ \text{stress}}} \underbrace{-\tau_{\text{io}}^x}_{\substack{\text{Ice-ocean}\\ \text{stress}}} \underbrace{+\frac{\partial \sigma_{21}}{\partial y}}_{\text{Ice rheology}}, \tag{9a}$$

$$\underbrace{\rho_{\text{i}} h_{\text{i}} \frac{\partial v_{\text{i}}}{\partial t}}_{\text{Tendency}} = \underbrace{-\rho_{\text{i}} h_{\text{i}} f u_{\text{i}}}_{\text{Coriolis}} \underbrace{+\tau_{\text{ai}}^y}_{\text{Wind stress}} \underbrace{-\tau_{\text{io}}^y}_{\text{Ice-ocean stress}} \underbrace{+\frac{\partial \sigma_{22}}{\partial y}}_{\text{Ice rheology}} \underbrace{-\rho_{\text{i}} h_{\text{i}} g \frac{\partial \eta}{\partial y}}_{\text{Sea surface slope}}, \tag{9b}$$

where η is the sea surface elevation and g is the gravitational acceleration. The sea surface slope term in Eq. 9b can be estimated from the meridional ocean momentum balance

$$g\frac{d\eta}{dy} = \frac{\tau_{\text{io}}^y}{\rho_{\text{o}}(h_{\text{o}}/2)} - f u_{\text{o}}^s. \tag{9c}$$

We further neglect changes in the sea ice growth rate due to thermodynamic processes (ice formation and melting). So the tendency of ice thickness depends only on the meridional advection of the sea ice,

$$\frac{\partial h_{\text{i}}}{\partial t} = -\frac{\partial}{\partial y}(h_{\text{i}} v_{\text{i}}). \tag{9d}$$

We find that in the 3D MITgcm simulations, tidal advection dominates the total ocean advection (Appendix B). So we substitute the total advection in this reduced-order model by tidal advection, which is derived following Loder (1980) (Appendix A3). In the 3D simulations we also ob-

serve that sea ice tends to drift with barotropic tides and diminishes the effect of tides on ice-ocean stress. Therefore we use the standard quadratic drag formulations for air-ice and ice-ocean stress in the reduced-order model, while modifying the ocean bottom stress and the topographic form stress by adding a mean tidal current (Appendix A4-5). Wind distribution and bathymetry of the reduced-order model are identical to those in the 3D simulations. Compared to the 3D model, the reduced-order model has identical wind distribution, and simplified model bathymetry without zonal variations. We integrate the model forward in time until it reaches the steady state, then compare the steady-state solutions with the 3D simulations. Details on the boundary conditions, model initialization, and numerical schemes are presented in Appendix A7-8.

b. Reduced-order simulations

Fig. 12a-b shows the ice and ocean zonal force balance for the reference simulation using the reduced-order model. Compared with MITgcm (Fig. 8a-b), this model successfully reproduces the salient features in the momentum budget, i.e., over the slope, sea ice internal stress divergence redistribute wind-input momentum (Fig. 12a), ice-ocean stress vanishes, and tidal advection is locally balanced by bottom frictional stress; over the shelf, topographic form stress balances the large momentum input from ice-ocean stress (Fig. 12b). There are a few disagreements between the two models with different complexity. The peak of the tidal advection slightly shifts onshore (Fig. 12b) in the reduced-order model because the troughs on the shelf modifies the strength of the tidal advection in MITgcm. In addition, the region of ice-ocean stress suppression is narrower in the reduced-order model compared with MITgcm. Overall, the reduced-order model can qualitatively and quantitatively reproduce the ocean and sea ice zonal force balance shown in the 3D MITgcm simulations. For the simulation with no tides, the results of the reduced-order model (Fig. 12e-f) are also consistent with that in MITgcm (Fig. 8c-d). We will discuss the remaining panels of Fig. 12 later in this section.

Fig. 13 compares the reduced-order simulations with the corresponding MITgcm simulations. Different colors denote experiments with varying parameters. This model does a fairly good job in predicting the maximum ocean surface and bottom velocities (Fig. 13a) and bottom frictional stress (Fig. 13d) over the slope. The theory developed by Bai et al. (2021) works very well in predicting the topographic form stress (Fig. 13d). The sea ice internal stress divergence and ice-ocean stress over the continental slope, which are the terms in the force balance that this study is most focused on, are accurately captured by the reduced-order model (Fig. 13c). Because of the simplified two-layer discretization, which is equivalent to assuming a linear vertical velocity profile in the ocean, this model is not able to represent the complex vertical structure of the slope current. Thus it substantially underestimates the baroclinic transport over the slope (Fig. 13b). Since this model has the assumption of zero time-averaged meridional flow in the ocean, it is not suitable for simulating cases with varying offshore buoyancy gradients. Understanding the effects of horizontal buoyancy gradients necessarily requires an understanding of the meridional overturning circulation as well, hence we leave it for further study.

As discussed in sections 3 and 4, there can be two mechanisms associated with the diminished ice-ocean stress: eddy suppression and tidal acceleration. To separate the effects of eddy suppression and tidal acceleration, we create four control experiments: with and without tides, and with and without eddy suppression. In this model, we can explicitly turn off eddy suppression by setting a horizontally uniform eddy diffusivity $K = 300$ m^2/s. A finite ice-ocean stress appears over the slope when eddies are not suppressed (Fig. 12g-h), which proves that eddy suppression is critical for the momentum balance of the ASC. Fig. 12c-d shows that tides strongly accelerate the lower level near the shelf break (125km offshore), decreasing the vertical velocity shear ($u_o^s - u_o^b$). Thus the momentum sink of the upper level, i.e., the isopycnal form stress, decreases (Eq. A5) near the shelf break, which accelerates the upper level. So the ice-ocean stress decreases near the shelf break with tides and no eddy suppression (Fig. 12d), though it remains significant over the continental slope. The ice-ocean stress can approach zero over the shelf break driven purely by tides, but this happens only when the tidal amplitude is sufficiently large.

We emphasize that little was done to "tune" this reduced-order model to the 3D simulations, largely because there are very few tunable parameters. Firstly, we choose an empirical constant to set the magnitude of the tidal advection in the reference case of the reduced-order model equivalent to the total ocean advection in the MITgcm reference simulation (Appendix A3). Secondly, the eddy parameterization is also tunable, but we choose to apply the eddy parameterization directly from Stewart and Thompson (2016) without any modification. The last tunable parameter is the minimum deformation rate Δ_0 in sea ice rheology (Appendix A6), which represents the minimum resistance of sea ice to external forcing. We regularize the ice deformation rate with this tunable parameter to prevent the ice internal stress from approaching infinity under the 1D assumption (Vancoppenolle et al. 2012). Increasing Δ_0 reduces the effective viscosity of sea ice (Appendix A8) and increases the magnitude of ice and ocean zonal velocities, but it does not qualitatively change the ice and ocean momentum budget.

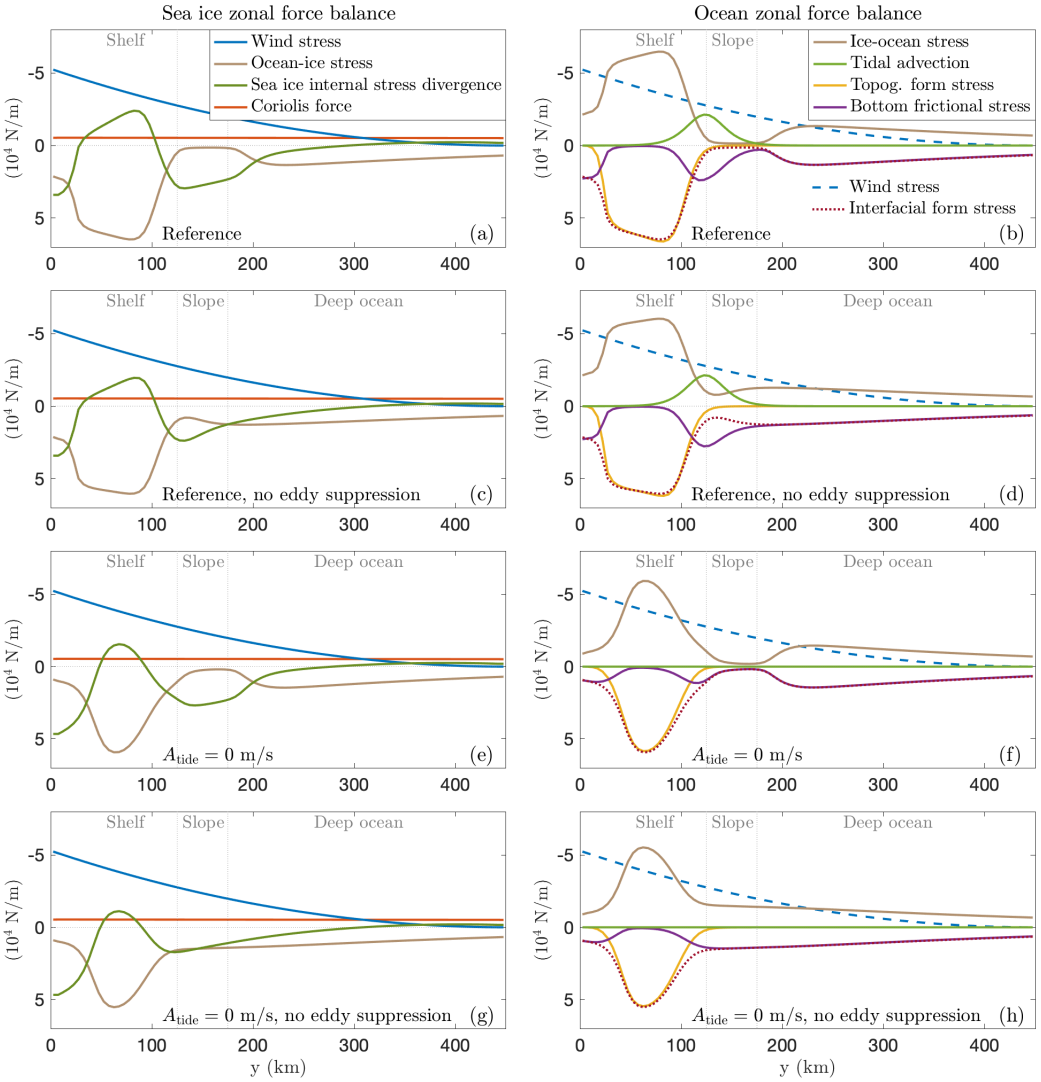

Figure 12. Reduced-order model simulation results. Sea ice and ocean zonal force balance for the reference case (a, b), and the no-tide case (e, f) with eddy suppression over the continental slope. Sea ice and ocean zonal force balance for the reference case (c, d), and the no-tide case (g, h) with a uniform eddy diffusivity $K = 300$ m^2/s, i.e., no eddy suppression over the continental slope.

6. Discussion and conclusions

In this study we utilized a high-resolution process-oriented model to investigate what controls the ice/ocean circulation and the pathways of momentum transfer in the ASC system with 100% sea ice cover. We also developed a reduced-order model of ice-ocean mechanical interactions to understand the role of eddy suppression over the continental slope. We emphasized the importance of topographic eddy suppression and sea ice momentum redistribution in the wind-ice-ASC system.

a. Key findings

In section 3 we showed the structure and intensity of the ASC in different control experiments, and highlighted the match of ice-ocean velocities over the slope (Fig. 4-5), indicating that local acceleration of the ocean by sea ice vanishes in this region.

We found that the intensity of the ASC increases with increasing tidal current amplitude, wind stress and slope steepness, and decreasing sea ice thickness (Fig. 4). The vertical structure of the ASC is primarily set by the offshore buoyancy gradient, varying from subsurface-intensified flow with a fresh shelf to a deep-reaching barotropic flow with a weak offshore buoyancy gradient, and to a bottom-intensified flow with a dense shelf (Fig. 5), in agreement

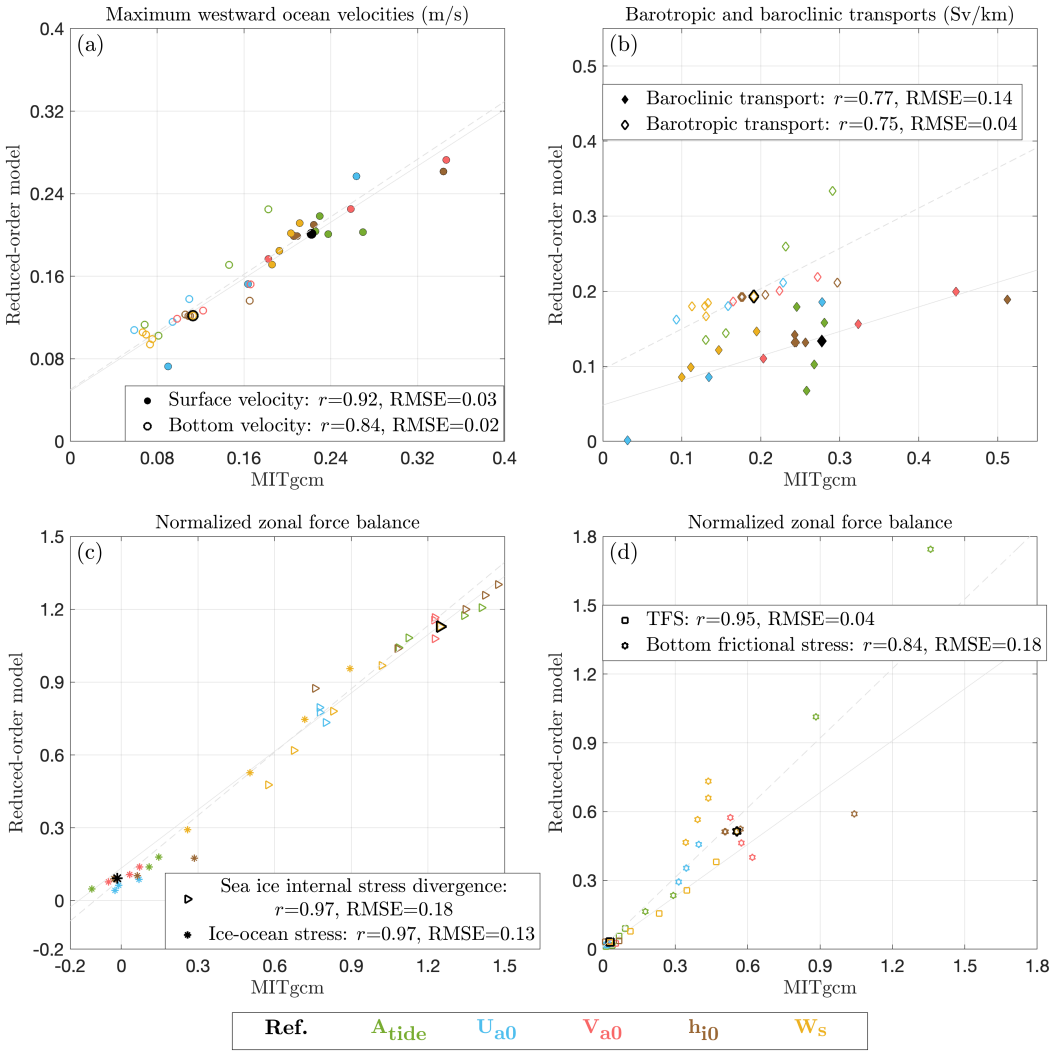

Figure 13. The reduced-order simulations compared with the 3D MITgcm simulations, where r is the linear correlation coefficient, and RMSE is the root-mean-square error. (a) Maximum westward ocean surface and bottom velocities in the slope region. (b) Mean westward barotropic and baroclinic transports over the continental slope. The barotropic transport is the ocean bottom velocity times ocean depth, and the baroclinic transport is the difference between the barotropic and the total transports. (c) Mean sea ice internal stress divergence and ice-ocean stress over the slope, normalized by the wind stress in the same region. (d) Mean topographic form stress and bottom frictional stress over the slope, normalized by the wind stress in the same region. The solid reference lines are the linear regression of the maximum westward ocean surface velocity, the baroclinic transport, normalized sea ice internal stress divergence, and normalized topographic form stress. The dashed reference lines are the linear regression of other scattered quantities.

with observations (e.g., Le Paih et al. 2020). We calculated the barotropic and baroclinic transports, and found that tides mainly change the barotropic transport, while wind forcing, sea ice thickness, slope steepness, and horizontal grid spacing predominantly affect the baroclinic transport (Fig. 6). Across a wide range of parameters, the zonal ocean surface velocity matches the velocity of sea ice over the continental slope. The approximate match of ice-ocean velocities occurs regardless of the strength of tidal amplitude, even when there are no tides (Fig. 4b). Exceptions occur in cases with very thin sea ice (Fig. 4e), dense outflows on the shelf (Fig. 5f), and very gentle topographic slope (Fig. 11c).

To determine the dynamical mechanisms that control the circulation and transport of the ASC, we analyzed the zonal momentum balance in section 4. Fig. 14 illustrates the mechanisms and directions of momentum transfer in the ASC in the equilibrium state. Wind transfers momentum to the sea ice via air-ice stress. Then the sea ice horizontally redistributes the wind-input momentum away from the continental slope by internal stress divergence, therefore playing a critical role in the momentum balance

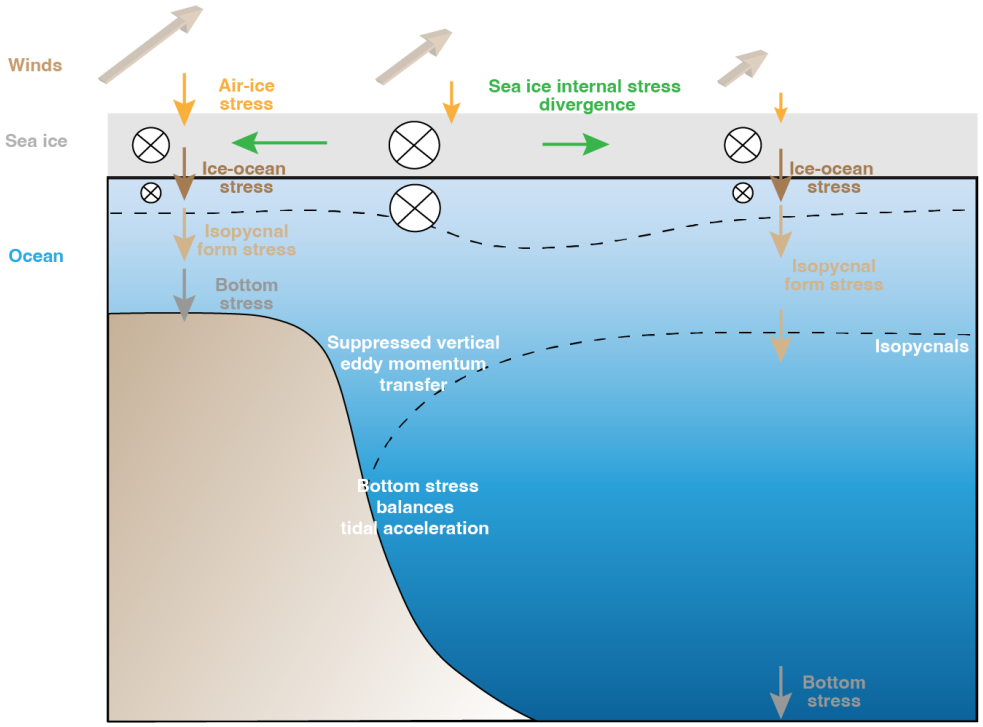

Figure 14. Schematic illustrating the momentum transfer in the wind-sea ice-ASC system in an equilibrium state, with exaggerated sea ice thickness. The 3D arrows denote northwestward surface winds, and other arrows denote the direction of zonal momentum transfer. The circles with crosses denote westward (along-slope, into the page) ice and ocean flow. The dashed curves denote isopycnals. Over the continental slope, eddies are suppressed and no momentum is transferred vertically via isopycnal form stress, leading to an equilibrium state in which the surface ocean velocity matches the ice velocity. Consequently, when the winds transfer westward momentum into the sea ice, it is redistributed horizontally away from the slope by sea ice internal stress divergence. Over the continental shelf and open ocean, ocean momentum sourced from ice-ocean stress is transferred downward by isopycnal form stress and finally removed by bottom frictional stress and topographic form stress.

of the ASC (Fig. 8a). Over the continental slope, the ASC is accelerated during the model spin-up until the speeds of sea ice and surface ocean coincide, and thus there is no ice-ocean momentum transfer. Tidal advection peaks over the slope and is locally balanced by bottom frictional stress (Fig. 8b). In the absence of tides, bottom frictional stress is very weak and balanced by a small amount of momentum input from ice-ocean stress and ocean advection (Fig. 8d). Over the continental shelf and the deep ocean, wind-input momentum is transferred downward by ice-ocean stress, then by isopycnal form stress, and is eventually dissipated at the sea floor by bottom frictional stress and topographic form stress. Ice-ocean momentum transfer becomes non-negligible for continental slopes that are much wider than is typical around Antarctica (Fig. 10c-d), or when dense water production and export occurs (Fig. 10e-f).

The reduced-order model verifies the hypothesis that eddy suppression is the key mechanism underlying the vanishing of the ice-ocean momentum transfer over the slope. As discussed in section 5, this reduced-order model accurately reproduces the zonal momentum budget in the 3D simulations (Fig. 13), and allows us to explicitly compare the cases with and without eddy suppression (Fig. 12). Our results show that over the continental shelf break, strong tidal acceleration reduces the ice-ocean stress, but the ice-ocean stress does not necessarily approach zero with the appearance of tides. Note that this contrasts with the suggestions of Stewart et al. (2019) and Flexas et al. (2015): when we turned on vertical momentum transfer over the slope by setting a uniform eddy diffusivity, the matching of sea ice and ocean surface velocities did not take place (Fig. 12c-d, g-h). Thus we concluded that the fundamental reason for the ice-ocean velocity match is the suppression of transient and standing eddies over the continental slope.

b. Limitations and implications

Our idealized model configuration enables efficient exploration of different dynamical mechanisms that control the circulation of the ice-ocean system, but the idealization also carries various limitations. For example, we neglect the baroclinicity of tidal currents, the complexity of varied tidal harmonic constituents, and the spacial variability in the tidal amplitudes, which may lead to underestimation of lateral momentum transfer in the ocean. As discussed

by Howard et al. (2004) and Koentopp et al. (2005), the baroclinic tidal currents contribute more to the variability of ice-ocean stress in the northern Weddell Sea and Scotia Sea, compared with barotropic currents. Moreover, the model imitates typical winter conditions around the East Antarctic margins with permanent sea ice coverage, excluding seasonal variations. Though the change of shelf stratification, sea ice concentration and thickness associated with the seasonal cycle can strongly affect the circulation of the ASC, as implied by previous studies as well as our simulation results. Note that our findings are not in dispute with the previously-established understanding that local winds are the primary momentum source for the ASC (e.g., Núñez-Riboni and Fahrbach 2009): in the equilibrium state, the vanishing of vertical momentum transfer in the core of the ASC does not imply that local winds are not the primary momentum source to the current as a whole. We expect the picture of momentum balance drawn in this study to be applicable to the annual-mean state of the real ASC (see Stewart et al. 2019). Further work will be required to understand the transient adjustment of circulation and momentum balance to changes in sea ice concentration, wind stress, and buoyancy forcing. Another caveat is that we made a simple choice to prescribe sea ice inflow velocity at the southern boundary, and thus ignored the reality that sea ice forms over and interacts with the continental shelf. The influence of the sea ice inflow on the momentum balance remains to be determined. Since our results agree with the findings of Stewart et al. (2019), derived from a realistic ocean/sea ice model, we expect the sea ice inflow to have little impact on the overall momentum balance. In addition, we expect the features of the momentum balance gained here to hold for sea ice concentrations higher than 80% based on Lepäranta (2011). There are also further limitations in the reduced-order model due to the one-dimensional assumption, the oversimplification of vertical discretization, the neglect of sea ice thermodynamics, cross-slope buoyancy forcing, diapycnal mixing, and meridional overturning circulation. Despite the fact that it carries various caveats, the reduced-order model helps us to better understand the continental slope dynamics, especially the role of eddy suppression.

This study has several implications for future research on the ASC, which are potentially relevant to the simulation of Arctic ice-ocean dynamics in the presence of continental slopes. First, a thorough understanding of the feedback between sea ice and ocean transport is required. On the one hand, changes in sea ice properties such as ice thickness, ice concentration, and ice drift speed have an influence on ice internal stress, which is critical to ice and ocean momentum balance, and thus can affect ocean transport. So sea ice will possibly affect the role of ASC as a barrier to prevent warm water intrusion and the melting of ice shelves. Meanwhile some ocean properties such as the lateral buoyancy gradient and tidal amplitude affect the concentration, thickness and transport of sea ice. We therefore emphasize the importance of coupled sea ice-ocean dynamics in future model studies of the ASC. In addition, resolving the eddies or otherwise representing their suppression over the continental slope is important. The large-scale zonal variations in forcing, geometry and state of the ASC should also be addressed in future research. Moreover, this study implies that tides influence the strength of the ASC, but do not qualitatively change the momentum balance of the ASC, since tidal advection is locally balanced by bottom frictional stress. Lastly, an important step forward from this study is the determination of the role of ASC momentum balance terms and their parameter dependences for the overturning circulation and cross-slope exchange.

Acknowledgments. This work is supported by the Faculty Early Career Development Program of the National Science Foundation, under award numbers OCE-1751386 and OPP-2023244, as well as awards OCE-2048590 and OPP-1643445. This work used the Extreme Science and Engineering Discovery Environment (XSEDE, Towns et al. 2014), which is supported by National Science Foundation grant number ACI-1548562. We thank the MITgcm team for their contribution to numerical modeling, and making their code available. Y. Si acknowledges the scholarship provided by China Scholarship Council that supports her study at UCLA. The authors sincerely thank Dr. Tore Hattermann and the other anonymous reviewer for their insightful suggestions and comments.

Data availability statement. The source code of the Massachusetts Institute of Technology General Circulation Model (MITgcm) is available at: http://mitgcm.org. The Matlab scripts used to generate, run, and analyze the MITgcm simulations, as well as the configurations of the MITgcm simulations are available at: http://doi.org/10.5281/zenodo.5048421. The source code, analysis code, and simulations of the reduced-order model are available at: http://doi.org/10.5281/zenodo.5048468.

APPENDIX A

Formulation of the reduced-order model

In section 5, we included a high-level overview of the reduced-order model. In this appendix we provide more details on the model configuration to better enable reproducibility, including conventional formulations developed by previous studies and our adaptations that make those formulations suitable for this reduced-order model.

1) Model bathymetry

The bathymetry of the reduced-order model is defined as

$$\eta_b(y) = -Z_s - \frac{H - H_{\text{shelf}}}{2} \tanh\left(\frac{y - Y_s}{W_s}\right). \tag{A1}$$

The description and values of the parameters are in Table 1. The ocean thickness in this model is $h_o(y) = -\eta_b(y)$.

2) Isopycnal form stress

The isopycnal form stress (IFS) represents the vertical momentum transfer by transient and standing eddies in the ocean. In this section we describe how to relate the IFS to the vertical velocity shear between the upper and the lower levels $(u_o^s - u_o^b)$.

The thermal wind relation indicates that the geostrophic velocity shear $\partial_z u_g \approx (u_o^s - u_o^b)/(\frac{1}{2}h_o)$ is proportional to the latitudinal (offshore) buoyancy gradient,

$$\partial_z u_g = \frac{g}{f\rho_0}\partial_y \bar{\rho} = -\frac{1}{f}\partial_y \bar{b}, \tag{A2}$$

where $b = -g(\rho/\rho_0 - 1)$ is the buoyancy, and a bar over the symbol represents its time average. The isopycnal slope s_{isop} is

$$s_{\text{isop}} \equiv -\frac{\partial_y \bar{b}}{\partial_z \bar{b}} = \frac{f\partial_z u_g}{\partial_z \bar{b}} \approx \frac{2f(u_o^s - u_o^b)}{N^2 h_o}, \tag{A3}$$

where $\partial_z \bar{b} = N^2$, and N is the mean stratification between the upper and the lower levels. We assume the horizontal variations in the vertical stratification are very weak, and use a constant stratification in the reduced-order simulations. The topographic parameter δ is

$$\delta \equiv \frac{s_b}{s_{\text{isop}}} \approx -\frac{N^2 h_o}{2f(u_o^s - u_o^b)}\partial_y h_o, \tag{A4}$$

where $s_b = -\partial_y h_o$ is the topographic slope.

Assuming that the vertical displacement of a given isopycnal η' is small, η' can be estimated as the buoyancy perturbation divided by the vertical buoyancy gradient, $\eta' \approx -b'/\partial_z \bar{b}$ (e.g., Vallis 2017). The fluctuation of the pressure gradient is related to the velocity perturbation using the geostrophic balance, $\partial_x p' = \rho_o f v'$. Therefore the IFS is

$$\begin{aligned} F_{\text{isop}} &= -\overline{\eta' p'_x} = \rho_o f \frac{\overline{v'b'}}{\partial_z \bar{b}} = -\rho_o f K \frac{\partial_y \bar{b}}{\partial_z \bar{b}} \\ &= \rho_o f K s_{\text{isop}} = 2\rho_o f^2 K \frac{(u_o^s - u_o^b)}{N^2 h_o}, \end{aligned} \tag{A5}$$

where the meridional eddy buoyancy flux is $\overline{v'b'} = -K\partial_y \bar{b}$, and K is the eddy diffusivity. We apply the eddy diffusivity parameterization following Stewart and Thompson (2013),

$$\begin{aligned} K = K_0 \Bigg[1 + \frac{1}{2}\sqrt{(1 - |\delta|)^2 + 4\gamma^2|\delta^2|} \\ - \frac{1}{2}\sqrt{(1 + |\delta|)^2 + 4\gamma^2|\delta^2|} \Bigg], \end{aligned} \tag{A6}$$

where $K_0 = 300$ m^2/s and $\gamma = 0.05$. Note that this parameterization doesn't generalize because it is an approximate fit to the diagnosed K in the reference simulation of Stewart and Thompson (2013), and can only be applied to simulations with a similar model setup. The key feature of this parameterization is that the eddy diffusivity K is greatly suppressed when $|\delta| \geq 1$.

3) Tidal acceleration

Following Loder (1980), the vertically averaged tidal velocities are

$$v_t = A_{\text{tide}} \frac{H}{h_o} \sin(\omega t). \tag{A7a}$$

$$u_t \approx A_{\text{tide}} \frac{H}{h_o} \sin(\omega t + \phi_t), \tag{A7b}$$

where ϕ_t is the phase lag between u_t and v_t. The meridional tidal velocity squared averaged over a tidal cycle is:

$$\overline{v_t^2} = \frac{1}{2}\left(A_{\text{tide}} \frac{H}{h_o}\right)^2. \tag{A8}$$

Tides enhance ocean bottom frictional stress and topographic form stress, so we add a mean tidal velocity to these terms, described in the following sections. We assume that when averaged over a tidal cycle, the momentum flux convergence in the ocean is mainly contributed by tidal advection (the rationale for this assumption will be described in Appendix B),

$$\begin{aligned} F_{\text{tide}} &= -\rho_o \frac{\partial}{\partial y} \int \overline{u'v'} dz \approx -\rho_o \frac{\partial}{\partial y} \int \overline{u_t v_t} dz \\ &= -s_b \rho_o \frac{1}{2}\left(A_{\text{tide}} \frac{H}{h_o}\right)^2 \cos\phi_t = -s_b \rho_o \overline{v_t^2} C \end{aligned} \tag{A9}$$

where $C = \cos\phi_t$ is an empirical constant representing the effect of phase lag ϕ_t between u_t and v_t on the magnitude of tidal advection. $C \approx -0.076$ is selected to set the magnitude of tidal advection in the reduced-order model equivalent to that of the 3D reference simulation.

4) Surface stresses

As discussed in section 5, the air-ice stress and ice-ocean stress have standard quadratic formulations, while

the ocean bottom stress is modified by tidal oscillations. As in the MITgcm simulations, the air-ice stress and the ice-ocean stress are

$$\boldsymbol{\tau_{ai}} = \rho_a C_{ai} |\boldsymbol{u_a}| \boldsymbol{u_a}, \tag{A10a}$$

$$\boldsymbol{\tau_{io}} = \rho_o C_{io} |\boldsymbol{u_i} - \boldsymbol{u_o}| (\boldsymbol{u_i} - \boldsymbol{u_o}), \tag{A10b}$$

where $\rho_a = 1.3$ kg/m^3 is the air density. The drag coefficients C_{ai}, C_{io}, and the wind speed distribution in the reduced-order model are consistent with the MITgcm simulations. The modified ocean bottom stress averaged over a tidal cycle is

$$\begin{aligned}\boldsymbol{\tau_b} &\approx \rho_o C_b |\boldsymbol{u_o^b} + \boldsymbol{u_t}| \boldsymbol{u_o^b} \approx \rho_o C_d \sqrt{(u_o^b)^2 + \overline{u_t^2} + \overline{v_t^2}}\, \boldsymbol{u_o^b} \\ &\approx \rho_o C_d \sqrt{(u_o^b)^2 + 2\overline{v_t^2}}\, \boldsymbol{u_o^b}.\end{aligned} \tag{A11}$$

5) Topographic form stress

Bai et al. (2021) have developed a barotropic, quasi-geostrophic theory for standing Rossby waves and extended their theory to a bathymetry with a continental shelf and slope. Following Bai et al. (2021), the topographic form stress in the reduced-order model is

$$F_{tfs} = -\frac{1}{2} \frac{\alpha_b^2}{(h_o^b)^2} \frac{r_b u_o^b f_0^2 / k_0^2}{(u_o^b + c_{k0})^2 + \left(\frac{r_b}{k_0 h_o^b}\right)^2}, \tag{A12}$$

where $k_0 = 2\pi/100$ km^{-1} is the wavenumber of the zonal bathymetric variation, r_b is the bottom drag coefficient, $c_{k0} = -\beta/k_0^2$ is the barotropic Rossby wave speed, $\beta = \beta_p + \beta_t = \beta_p + f s_b / h_o$ is the sum of the planetary beta parameter and the topographic beta parameter. α_b is the along-slope variation of the bathymetry (the difference in elevation between the bumps and the troughs, Fig. 2), obtained from the corresponding 3D MITgcm model bathymetry. Similar to the modified ocean bottom stress (Eq. A11), we add the mean tidal velocity to the bottom drag coefficient to simulate the effect of tides on topographic form stress,

$$r_b = C_d \sqrt{(u_o^b)^2 + 2\overline{v_t^2}}. \tag{A13}$$

In the reduced-order simulations, the first term in the denominator $(u_o^b + c_{k0})^2$ in Eq. A12 is about 300 times larger than the second term $(r_b/k_0/h_o^b)^2$.

6) Sea ice rheology

We use a standard viscous-plastic (VP) rheology following Hibler (1979) and Heorton et al. (2014), and derive the sea ice rheology terms in the ice momentum equation under the assumptions (i)-(iii) in section 5. The components of the two-dimensional sea ice internal stress tensor $\boldsymbol{\sigma}$ are expressed as

$$\sigma_{ij} = 2\eta \dot{\epsilon}_{ij} + (\zeta - \eta) \dot{\epsilon}_{kk} \delta_{ij} - \frac{1}{2} p \delta_{ij}, \tag{A14}$$

where δ_{ij} is the Kronecker delta. $\dot{\epsilon}_{ij} = \frac{1}{2}\left(\frac{\partial u_i}{\partial x_j} + \frac{\partial u_j}{\partial x_i}\right)$ denote the components of the strain-rate tensor (i and j represent the zonal and the meridional directions), and $\dot{\epsilon}_{kk} = \dot{\epsilon}_{11} + \dot{\epsilon}_{22}$ using the Einstein summation convention. $\zeta = \frac{p}{2\Delta}$ is the bulk viscosity. $\eta = \frac{\zeta}{e^2}$ is the shear viscosity. $e = 2$ is the dimensionless elastic modulus in ice rheology, which defines the elliptical aspect ratio. The ice compressive strength is $p = p^\star h_i G(A_i) = p^\star h_i \exp[-c(1 - A_i)]$, where $p^* = 4 \times 10^4$ N/m^2 is the ice pressure constant, and c is an empirical constant (Hibler 1979). We assume the sea ice concentration $A_i = 1$ in all of the reduced-order simulations, so $p = p^* h_i$. The sea ice deformation rate is defined as

$$\Delta = \left[(1 + e^{-2})(\dot{\epsilon}_{11}^2 + \dot{\epsilon}_{22}^2) + 4e^{-2}\dot{\epsilon}_{12}^2 + 2(1 - e^{-2})\dot{\epsilon}_{11}\dot{\epsilon}_{22}^2\right]^{1/2}. \tag{A15}$$

Under the assumptions (i)-(iii) in section 5,

$$\dot{\epsilon}_{11} = 0,\ \dot{\epsilon}_{22} = \frac{\partial v_i}{\partial y},\ \dot{\epsilon}_{12} = \dot{\epsilon}_{21} = \frac{1}{2}\frac{\partial u_i}{\partial y}. \tag{A16}$$

When Δ approaches zero, we regularize $\boldsymbol{\sigma}$ by setting $\Delta_0 = 10^{-6} s^{-1}$, which is the minimum deformation rate for ice rheology to prevent the viscosity from approaching infinity (Vancoppenolle et al. 2012),

$$\Delta = \sqrt{\Delta_0^2 + \left[(1 + e^{-2})\left(\frac{\partial v_i}{\partial y}\right)^2 + e^{-2}\left(\frac{\partial u_i}{\partial y}\right)^2\right]}. \tag{A17}$$

The sea ice internal stress divergence is $\partial_x \sigma_{11} + \partial_y \sigma_{21} = \partial_y \sigma_{21}$ in the zonal ice momentum equation, and $\partial_x \sigma_{12} + \partial_y \sigma_{22} = \partial_y \sigma_{22}$ in the meridional ice momentum equation, where the ice internal stress tensor components are

$$\sigma_{21} = 2\eta \dot{\epsilon}_{21} = \eta \frac{\partial u_i}{\partial y} = \frac{p^* h_i}{2e^2 \Delta} \frac{\partial u_i}{\partial y}, \tag{A18a}$$

$$\begin{aligned}\sigma_{22} &= 2\eta \dot{\epsilon}_{22} + (\zeta - \eta)(\dot{\epsilon}_{11} + \dot{\epsilon}_{22}) - \frac{p}{2} \\ &= (\zeta + \eta)\frac{\partial v_i}{\partial y} - \frac{p}{2} = (1 + e^{-2})\frac{p^* h_i}{2\Delta}\frac{\partial v_i}{\partial y} - \frac{p^* h_i}{2}.\end{aligned} \tag{A18b}$$

7) Boundary conditions and initialization

Similar to the MITgcm configuration, we assume a free-drift ice boundary for the reduced-order model. We solve Eq. 2 for given boundary ice thickness (h_{i0}) and wind speeds to get the sea ice velocities at the southern boundary (U_{i0}, V_{i0}). We linearly extrapolate u_o^s and u_o^b at the southern boundary, and u_i, v_i, h_i, u_o^s and u_o^b at the northern boundary.

The reduced-order model is initialized with a uniform ice thickness h_{i0}, a uniform meridional ice velocity V_{i0}, and a stationary ocean.

8) Grid spacing, numerical schemes and time step

The reduced-order model is implemented with Arakawa C-grids (Arakawa and Lamb 1977) to enforce conservation of mass with a second-order center-in-space scheme for space discretization. The zonal (u-grid) and meridional (v-grid) velocities are staggered in space with u-grid defined at the grid center and v-grid defined at the grid corners. The sea ice thickness is defined on the u-grid. We neglect advection terms in the momentum equations and use the upwind scheme for advection in the sea ice thickness equation.

The time step of the reduced-order model is limited by sea ice internal stress divergence. To estimate the maximum time step, we apply the scale analysis below:

$$\frac{du_i}{dt_{max}} \sim \frac{1}{h_i}\frac{d\sigma_{21}}{dy} \sim \frac{p^\star}{2\rho_i e^2 \Delta_0}\frac{du_i}{dy^2} \sim \nu_{eff}\frac{du_i}{dy^2}, \tag{A19}$$

where $\nu_{eff} = p^\star/(2\rho_i e^2\Delta_0)$ is the effective viscosity, and $dt_{max} \sim dy^2/\nu_{eff}$ is the maximum time step. While numerical models are commonly implemented with additional solvers (such as LSR in MITgcm) to deal with the requirement of extremely small time step associated with sea ice rheology, we prefer simple time stepping method because this model is computationally inexpensive. The maximum time step required by the forward Euler method is larger than that of the third-order Adams-Bashforth method (AB3) in the experiment, so we implement the forward Euler method for time stepping.

In the reduced-order simulations, the meridional grade spacing is 5 km, and the required time step is 1.8 s ($dt_{max} \sim$ 4.7 s). The spatial convergence of the reduced-order model is examined using 2-km spacing and a 0.25-s time step, and we find that using this higher spatial resolution has little effect on the solution (results not shown). Each simulation reaches its equilibrium state after a 300-day integration, and is run for a total of 500 days to perform analysis.

APPENDIX B

Decomposition of the total advection for the 3D MITgcm simulations

This appendix includes the methods to temporally decompose the total zonal ocean advection into three components: tidal, eddy and mean, following Stewart et al. (2019), as well as the rationale for representing the total advection by its tidal component in the reduced-order model.

The zonal ocean momentum advection is expressed as

$$\begin{aligned} -(\boldsymbol{u}\cdot\boldsymbol{\nabla})u &= -(u\partial_x u + v\partial_y u + w\partial_z u) \\ &= \underbrace{v(\partial_x v - \partial_y u)}_{\text{Vorticity Adv.}} \quad \underbrace{-w\partial_z u}_{\text{Vertical Adv.}} \quad \underbrace{-\partial_x(u^2+v^2)/2}_{\text{Kinetic Energy Gradient}}, \end{aligned} \tag{B1}$$

where *Adv.* is the abbreviation for *Advection*. The following operators are defined for decomposition, representing an average over two tidal periods (1 model day) and an average of *daily averaged* quantities over 5 model years.

$$\overline{\bullet}^T = \frac{1}{1\text{ day}}\int_{t_0}^{t_0+1\text{ day}} \bullet\, dt, \tag{B2a}$$

$$\overline{\bullet}^E = \frac{1}{5\text{ years}}\int_{t_0}^{t_0+5\text{ years}} \overline{\bullet}^T\, dt. \tag{B2b}$$

The subscript m, e and t denote time-mean, and the eddy and tidal components of the quantity, respectively (Stewart et al. 2019).

$$\boldsymbol{u}_m = \overline{\overline{\boldsymbol{u}}^T}^E = \overline{\boldsymbol{u}}^E, \tag{B3a}$$

$$\boldsymbol{u}_e = \overline{\boldsymbol{u}}^T - \overline{\boldsymbol{u}}^E, \tag{B3b}$$

$$\boldsymbol{u}_t = \boldsymbol{u} - \boldsymbol{u}_m - \boldsymbol{u}_e = \boldsymbol{u} - \overline{\boldsymbol{u}}^T. \tag{B3c}$$

We follow the spacial discretization of the momentum advection implemented in MITgcm, and calculate the mean, eddy, and tidal advection using the 5-year averaged diagnostics u_m, v_m, w_m, Total Adv., and the daily averaged diagnostics $\bar{u}^T$, $\bar{v}^T$ and $\bar{w}^T$.

$$\text{Mean Adv.} = v_m(\partial_x v_m - \partial_y u_m) - w_m\partial_z u_m - \partial_x(u_m^2+v_m^2)/2, \tag{B4a}$$

$$\begin{aligned} \text{Eddy Adv.} &= \overline{v_e(\partial_x v_e - \partial_y u_e)}^E - \overline{w_e\partial_z u_e}^E - \overline{\partial_x(u_e^2+v_e^2)/2}^E \\ &= \overline{\bar{v}^T(\partial_x \bar{v}^T - \partial_y \bar{u}^T)}^E - \overline{\bar{w}^T\partial_z \bar{u}^T}^E - \overline{\partial_x({\bar{u}^T}^2+{\bar{v}^T}^2)/2}^E \\ &\quad - \text{Mean Adv.}, \end{aligned} \tag{B4b}$$

$$\text{Tidal Adv.} = \text{Total Adv.} - \text{Mean Adv.} - \text{Eddy Adv.} \tag{B4c}$$

Note that although we endeavored to improve the algorithm, the decomposition is likely somewhat imperfect due to the complexity of reproducing the MITgcm discretization.

Fig. B1 shows the zonally and vertically integrated zonal momentum advection for the reference case and the cases with very dense shelf and very fresh shelf. For the simulations with a moderate offshore buoyancy gradient similar to the reference case, the ocean advection is primarily contributed by tidal advection. In the very dense shelf case ($\Delta S = 0.62$ psu), strong vertical stratification intensifies the tidal momentum flux convergence and tidal rectification (Chen and Beardsley 1995). Baroclinic instabilities

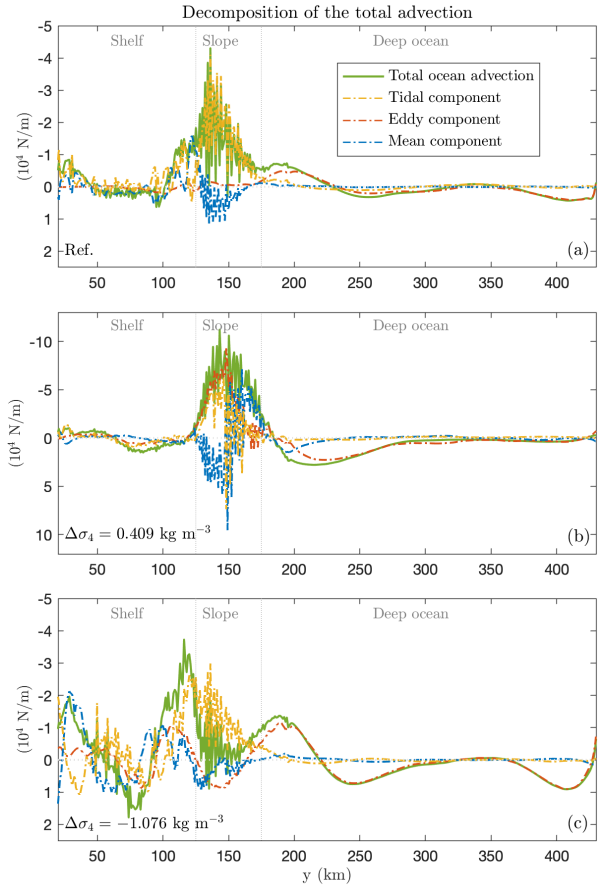

Figure B1. Temporal decomposition of the total ocean advection in the reference simulation (a), the very dense shelf case (b), and the very fresh shelf case (c). Note that the y-axis limits are different in the three panels.

arise from the sharp offshore buoyancy gradient and enhance the eddy advection. In the very fresh shelf case ($\Delta S = -1.17$ psu), the mean and eddy components play a role in setting the total advection over the edge of the continental shelf (100-120 km offshore). Except for the cases with extreme offshore buoyancy gradient, total advection is intensified over the continental slope, and is dominated by the tidal component. This supports the interpretation of the advective forcing as tidal rectification in almost all experiments. Hence we parameterize the tidal advection in the reduced-order model, and neglect other advection components to simplify and stabilize the model.

APPENDIX C

3D Model bathymetry

In this appendix we describe the formulation of the bathymetry used in the 3D MITgcm simulations. The bathymetry $z = \eta_b(x, y)$ is defined by equation C1, where $\mathcal{H}[\cdot]$ denotes the Heaviside step function. The values of the topographic parameters are listed in Table 1.

References

Amante, C., and B. W. Eakins, 2009: ETOPO1 1 Arc-Minute Global Relief Model: Procedures, Data Sources and Analysis. NOAA Technical Memorandum NESDIS NGDC-24. *National Geophysical Data Center, NOAA*, URL https://doi.org/10.7289/V5C8276M.

Arakawa, A., and V. R. Lamb, 1977: Computational design of the basic dynamical processes of the UCLA general circulation model. *General circulation models of the atmosphere*, **17 (Supplement C)**, 173–265, URL https://doi.org/10.1016/B978-0-12-460817-7.50009-4.

Armitage, T. W. K., R. Kwok, A. F. Thompson, and G. Cunningham, 2018: Dynamic topography and sea level anomalies of the Southern Ocean: Variability and teleconnections. *J. Geophys. Res.: Oceans*, **123 (1)**, 613–630, URL https://doi.org/10.1002/2017JC013534.

Bai, Y., Y. Wang, and A. L. Stewart, 2021: Does Topographic Form Stress Impede Prograde Ocean Currents? *J. Phys. Oceanogr.*, URL https://doi.org/10.1175/JPO-D-20-0189.1.

Barth, A., and Coauthors, 2015: Assimilation of sea surface temperature, sea ice concentration and sea ice drift in a model of the Southern Ocean. *Ocean Modell.*, **93**, 22–39, URL https://doi.org/10.1016/j.ocemod.2015.07.011.

Bintanja, R., G. J. van Oldenborgh, S. Drijfhout, B. Wouters, and C. Katsman, 2013: Important role for ocean warming and increased ice-shelf melt in Antarctic sea-ice expansion. *Nat. Geosci.*, **6 (5)**, 376–379, URL https://doi.org/10.1038/NGEO1767.

Blumsack, S. L., and P. J. Gierasch, 1972: Mars: The effects of topography on baroclinic instability. *J. Atmos. Sci.*, **29 (6)**, 1081–1089, URL https://doi.org/10.1175/1520-0469(1972)029<1081:MTEOTO>2.0.CO;2.

Brink, K., 1991: Coastal-trapped waves and wind-driven currents over the continental shelf. *Annu. Rev. Fluid Mech.*, **23 (1)**, 389–412, URL https://doi.org/10.1146/annurev.fl.23.010191.002133.

Brink, K., and S. Lentz, 2010: Buoyancy arrest and bottom Ekman transport. Part II: Oscillating flow. *J. Phys. Oceanogr.*, **40 (4)**, 636–655, URL https://doi.org/10.1175/2009JPO4267.1.

Brink, K. H., 2010: Topographic rectification in a forced, dissipative, barotropic ocean. *J. Mar. Res.*, **68 (3-4)**, 337–368, URL https://doi.org/10.1357/002224010794657209.

Brink, K. H., 2011: Topographic rectification in a stratified ocean. *J. of Mar. Res.*, **69 (4-5)**, 483–499, URL https://doi.org/10.1357/002224011799849354.

Brink, K. H., 2013: Instability of a tidal mixing front in the presence of realistic tides and mixing. *J. Mar. Res.*, **71 (3)**, 227–251, URL https://doi.org/10.1357/002224013807719473.

Bull, C. Y. S., A. Jenkins, N. C. Jourdain, I. Vaňková, P. R. Holland, P. Mathiot, U. Hausmann, and J.-B. Sallée, 2021: Remote control of Filchner-Ronne Ice Shelf melt rates by the Antarctic Slope Current. *J. Geophys. Res.: Oceans*, **126 (2)**, e2020JC016 550, URL https://doi.org/10.1029/2020JC016550.

Chen, C., and R. C. Beardsley, 1995: A numerical study of stratified tidal rectification over finite-amplitude banks. Part I: Symmetric banks. *J. Phys. Oceanogr.*, **25 (9)**, 2090–2110, URL https://doi.org/10.1175/1520-0485(1995)025%3C2090:ANSOST%3E2.0.CO;2.

$$\eta_b(x,y) = -Z_s - \frac{H_{\text{trough}}}{2}(N_{\text{trough}} - 1) - h_{\text{trough}}(x,y) - \frac{H - H_{\text{shelf}} - 2h_{\text{trough}}(x,y)}{2}\tanh\left(\frac{y - Y_s}{W_s}\right), \tag{C1a}$$

$$h_{\text{trough}}(x,y) = \sum_{n=1}^{N_{\text{trough}}} \mathcal{H}\left[y - Y_{\text{trough}}\right] H_{\text{trough}} \exp\left(-\left(\frac{x - L_x(2n - 1 - N_{\text{trough}})/2/N_{\text{trough}}}{W_{\text{trough}}}\right)^4\right) \ldots \times\left(1 - \frac{1}{2}\mathcal{H}\left[(Y_s - W_s) - y\right]\left(1 + \cos\left(\pi\frac{y - Y_{\text{trough}}}{Y_s - W_s - Y_{\text{trough}}}\right)\right)\right). \tag{C1b}$$

Cherian, D. A., and K. H. Brink, 2018: Shelf flows forced by deep-ocean anticyclonic eddies at the shelf break. *J. Phys. Oceanogr.*, **48 (5)**, 1117–1138, URL https://doi.org/10.1175/JPO-D-17-0237.1.

Fer, I., E. Darelius, and K. B. Daae, 2016: Observations of energetic turbulence on the Weddell Sea continental slope. *Geophys. Res. Lett.*, **43 (2)**, 760–766, URL https://doi.org/10.1002/2015GL067349.

Ferreira, D., and J. Marshall, 2006: Formulation and implementation of "residual-mean" ocean circulation model. *Ocean Modell.*, **13 (1)**, 86–107, URL https://doi.org/10.1016/j.ocemod.2005.12.001.

Flexas, M. d. M., M. P. Schodlok, L. Padman, D. Menemenlis, and A. H. Orsi, 2015: Role of tides on the formation of the Antarctic Slope Front at the Weddell-Scotia Confluence. *J. Geophys. Res.: Oceans*, **120 (5)**, 3658–3680, URL https://doi.org/10.1002/2014JC010372.

Garreau, P., and R. Maze, 1992: Tidal rectification and mass transport over a shelf break: A barotropic frictionless model. *J. Phys. Oceanogr.*, **22 (7)**, 719–731, URL https://doi.org/10.1175/1520-0485(1992)022<0719:TRAMTO>2.0.CO;2.

Gent, P. R., and J. C. Mcwilliams, 1990: Isopycnal mixing in ocean circulation models. *J. Phys. Oceanogr.*, **20 (1)**, 150–155, URL https://doi.org/10.1175/1520-0485(1990)020<0150:IMIOCM>2.0.CO;2.

Gent, P. R., J. Willebrand, T. J. McDougall, and J. C. McWilliams, 1995: Parameterizing eddy-induced tracer transports in ocean circulation models. *J. Phys. Oceanogr.*, **25 (4)**, 463–474, URL https://doi.org/10.1175/1520-0485(1995)025<0463:PEITTI>2.0.CO;2.

Gill, A. E., 1973: Circulation and bottom water production in the Weddell Sea. *Deep Sea Res. and Oceanographic Abstracts*, Elsevier, Vol. 20, 111–140, URL https://doi.org/10.1016/0011-7471(73)90048-X.

Goddard, P. B., C. O. Dufour, J. Yin, S. M. Griffies, and M. Winton, 2017: CO2-induced ocean warming of the Antarctic continental shelf in an eddying global climate model. *J. Geophys. Res.: Oceans*, **122 (10)**, 8079–8101, URL https://doi.org/10.1002/2017JC012849.

Hattermann, T., 2018: Antarctic thermocline dynamics along a narrow shelf with easterly winds. *J. Phys. Oceanogr.*, **48 (10)**, 2419–2443, URL https://doi.org/10.1175/JPO-D-18-0064.1.

Hazel, J. E., and A. L. Stewart, 2019: Are the near-Antarctic easterly winds weakening in response to enhancement of the Southern Annular Mode? *J. Clim.*, **32 (6)**, 1895–1918, URL https://doi.org/10.1175/JCLI-D-18-0402.1.

Heorton, H. D. B. S., D. L. Feltham, and J. C. R. Hunt, 2014: The response of the sea ice edge to atmospheric and oceanic jet formation. *J. Phys. Oceanogr.*, **44 (9)**, 2292–2316, URL https://doi.org/10.1175/JPO-D-13-0184.1.

Hetland, R. D., 2017: Suppression of baroclinic instabilities in buoyancy-driven flow over sloping bathymetry. *J. Phys. Oceanogr.*, **47 (1)**, 49–68, URL https://doi.org/10.1175/JPO-D-15-0240.1.

Heywood, K. J., R. A. Locarnini, R. D. Frew, P. F. Dennis, and B. A. King, 1998: Transport and water masses of the Antarctic Slope Front system in the eastern Weddell Sea. *Ocean, Ice, and Atmosphere: Interactions at the Antarctic Continental Margin, Antarct. Res. Ser*, **75**, 203–214, URL https://doi.org/10.1029/AR075p0203.

Heywood, K. J., and Coauthors, 2014: Ocean processes at the Antarctic continental slope. *Philos. Trans. R. Soc. London, Ser. A*, **372 (2019)**, 20130047, URL https://doi.org/10.1098/rsta.2013.0047.

Hibler, W. D., III, 1979: A dynamic thermodynamic sea ice model. *J. Phys. Oceanogr.*, **9 (4)**, 815–846, URL https://doi.org/10.1175/1520-0485(1979)009<0815:ADTSIM>2.0.CO;2.

Hibler, W. D., III, 1980: Modeling a variable thickness sea ice cover. *Mon. Weather Rev.*, **108 (12)**, 1943–1973, URL https://doi.org/10.1175/1520-0493(1980)108<1943:MAVTSI>2.0.CO;2.

Holland, P. R., 2014: The seasonality of Antarctic sea ice trends. *Geophys. Res. Lett.*, **41 (12)**, 4230–4237, URL https://doi.org/10.1002/2014GL060172.

Holland, P. R., R. E. Hewitt, and M. M. Scase, 2014: Wave breaking in dense plumes. *J. Phys. Oceanogr.*, **44 (2)**, 790–800, URL https://doi.org/10.1175/JPO-D-13-0110.1.

Holland, P. R., and R. Kwok, 2012: Wind-driven trends in Antarctic sea-ice drift. *Nat. Geosci.*, **5 (12)**, 872–875, URL https://doi.org/10.1038/NGEO1627.

Howard, E., A. McC. Hogg, S. Waterman, and D. P. Marshall, 2015: The injection of zonal momentum by buoyancy forcing in a southern ocean model. *J. Phys. Oceanogr.*, **45 (1)**, 259–271, URL https://doi.org/10.1175/JPO-D-14-0098.1.

Howard, S., J. Hyatt, and L. Padman, 2004: Mixing in the pycnocline over the western Antarctic Peninsula shelf during Southern Ocean GLOBEC. *Deep Sea Res. Part II*, **51 (17-19)**, 1965–1979, URL https://doi.org/10.1016/j.dsr2.2004.08.002.

Huneke, W. G. C., A. Klocker, and B. K. Galton-Fenzi, 2019: Deep bottom mixed layer drives intrinsic variability of the Antarctic Slope Front. *J. Phys. Oceanogr.*, **49 (12)**, 3163–3177, URL https://doi.org/10.1175/JPO-D-19-0044.1.

Huthnance, J., 1973: Tidal current asymmetries over the Norfolk Sandbanks. *Estuarine Coastal Mar. Sci.*, **1 (1)**, 89–99, URL https://doi.org/10.1016/0302-3524(73)90061-3.

Isachsen, P. E., 2011: Baroclinic instability and eddy tracer transport across sloping bottom topography: How well does a modified Eady

model do in primitive equation simulations? *Ocean Modell.*, **39 (1-2)**, 183–199, URL https://doi.org/10.1016/j.ocemod.2010.09.007.

Jacobs, S. S., 1991: On the nature and significance of the Antarctic Slope Front. *Mar. Chem.*, **35 (1-4)**, 9–24, URL https://doi.org/10.1016/S0304-4203(09)90005-6.

Koentopp, M., O. Eisen, C. Kottmeier, L. Padman, and P. Lemke, 2005: Influence of tides on sea ice in the Weddell Sea: Investigations with a high-resolution dynamic-thermodynamic sea ice model. *J. Geophys. Res.: Oceans*, **110 (C2)**, URL https://doi.org/10.1029/2004JC002405.

Kowalik, Z., and A. Y. Proshutinsky, 1995: Topographic enhancement of tidal motion in the western Barents Sea. *J. Geophys. Res.: Oceans*, **100 (C2)**, 2613–2637, URL https://doi.org/10.1029/94JC02838.

Lamb, K. G., 2014: Internal wave breaking and dissipation mechanisms on the continental slope/shelf. *Annu. Rev. Fluid Mech.*, **46**, 231–254, URL https://doi.org/10.1146/annurev-fluid-011212-140701.

Le Paih, N., T. Hattermann, O. Boebel, T. Kanzow, C. Lüpkes, G. Rohardt, V. Strass, and S. Herbette, 2020: Coherent seasonal acceleration of the Weddell sea boundary current system driven by upstream winds. *J. Geophys. Res.: Oceans*, **125 (10)**, e2020JC016 316, URL https://doi.org/10.1029/2020JC016316.

Leppäranta, M., 2011: *The drift of sea ice*. Springer Science & Business Media, URL https://doi.org/10.1007/978-3-642-04683-4.

Loder, J. W., 1980: Topographic rectification of tidal currents on the sides of Georges Bank. *J. Phys. Oceanogr.*, **10 (9)**, 1399–1416, URL https://doi.org/10.1175/1520-0485(1980)010<1399:TROTCO>2.0.CO;2.

Losch, M., A. Fuchs, J.-F. Lemieux, and A. Vanselow, 2014: A parallel Jacobian-free Newton–Krylov solver for a coupled sea ice-ocean model. *J. Comput. Phys.*, **257**, 901–911, URL https://doi.org/10.1016/j.jcp.2013.09.026.

Losch, M., D. Menemenlis, J.-M. Campin, P. Heimbach, and C. Hill, 2010: On the formulation of sea-ice models. Part 1: Effects of different solver implementations and parameterizations. *Ocean Modell.*, **33 (1)**, 129–144, URL https://doi.org/10.1016/j.ocemod.2009.12.008.

Lüpkes, C., and V. M. Gryanik, 2015: A stability-dependent parametrization of transfer coefficients for momentum and heat over polar sea ice to be used in climate models. *J. Geophys. Res.: Atmos.*, **120 (2)**, 552–581, URL https://doi.org/10.1002/2014JD022418.

Lüpkes, C., V. M. Gryanik, J. Hartmann, and E. L. Andreas, 2012: A parametrization, based on sea ice morphology, of the neutral atmospheric drag coefficients for weather prediction and climate models. *J. Geophys. Res.: Atmos.*, **117 (D13)**, URL https://doi.org/10.1029/2012JD017630.

Marshall, J., A. Adcroft, C. Hill, L. Perelman, and C. Heisey, 1997a: A finite-volume, incompressible Navier Stokes model for studies of the ocean on parallel computers. *J. Geophys. Res.*, **102**, 5753–5766, URL https://doi.org/10.1029/96JC02775.

Marshall, J., C. Hill, L. Perelman, and A. Adcroft, 1997b: Hydrostatic, quasi-hydrostatic, and nonhydrostatic ocean modeling. *J. Geophys. Res.*, **102**, 5733–5752, URL https://doi.org/10.1029/96JC02776.

Masich, J., T. K. Chereskin, and M. R. Mazloff, 2015: Topographic form stress in the S outhern O cean S tate E stimate. *J. Geophys. Res.: Oceans*, **120 (12)**, 7919–7933, URL https://doi.org/10.1002/2015JC011143.

Masich, J., M. R. Mazloff, and T. K. Chereskin, 2018: Interfacial form stress in the southern ocean state estimate. *J. Geophys. Res.: Oceans*, **123 (5)**, 3368–3385, URL https://doi.org/10.1029/2018JC013844.

Mathiot, P., H. Goosse, T. Fichefet, B. Barnier, and H. Gallée, 2011: Modelling the seasonal variability of the Antarctic Slope Current. *Ocean Sci.*, **7 (4)**, 455–470, URL https://doi.org/10.5194/os-7-455-2011.

McDougall, T. J., D. R. Jackett, D. G. Wright, and R. Feistel, 2003: Accurate and computationally efficient algorithms for potential temperature and density of seawater. *J. Atmos. Oceanic Technol.*, **20 (5)**, 730–741, URL https://doi.org/10.1175/1520-0426(2003)20<730:AACEAF>2.0.CO;2.

McWilliams, J. C., 2008: The nature and consequences of oceanic eddies. *Ocean modeling in an eddying regime*, **177**, 5–15, URL http://www.ccpo.odu.edu/~klinck/Reprints/PDF/mcwilliamsOMER2008.pdf.

Moorman, R., A. K. Morrison, and A. McC. Hogg, 2020: Thermal Responses to Antarctic Ice Shelf Melt in an Eddy-Rich Global Ocean–Sea Ice Model. *J. Clim.*, **33 (15)**, 6599–6620, URL https://doi.org/10.1175/JCLI-D-19-0846.1.

Muench, R., L. Padman, A. Gordon, and A. Orsi, 2009: A dense water outflow from the Ross Sea, Antarctica: Mixing and the contribution of tides. *J. Mar. Syst.*, **77 (4)**, 369–387, URL https://doi.org/10.1016/j.jmarsys.2008.11.003.

Munk, W. H., and E. Palmén, 1951: Note on the dynamics of the antarctic circumpolar current 1. *Tellus*, **3 (1)**, 53–55, URL https://doi.org/10.1111/j.2153-3490.1951.tb00776.x.

Mysak, L. A., 1980: Topographically trapped waves. *Annu. Rev. Fluid Mech.*, **12 (1)**, 45–76, URL https://doi.org/10.1146/annurev.fl.12.010180.000401.

Nakayama, Y., K. I. Ohshima, Y. Matsumura, Y. Fukamachi, and H. Hasumi, 2014: A Numerical Investigation of Formation and Variability of Antarctic Bottom Water off Cape Darnley, East Antarctica. *J. Phys. Oceanogr.*, **44 (11)**, 2921–2937, URL https://doi.org/10.1175/JPO-D-14-0069.1.

Naughten, K. A., K. J. Meissner, B. K. Galton-Fenzi, M. H. England, R. Timmermann, and H. H. Hellmer, 2018: Future projections of Antarctic ice shelf melting based on CMIP5 scenarios. *J. Clim.*, **31 (13)**, 5243–5261, URL https://doi.org/10.1175/JCLI-D-17-0854.1.

Naveira Garabato, A. C., and Coauthors, 2019: Phased response of the subpolar Southern Ocean to changes in circumpolar winds. *Geophys. Res. Lett.*, **46 (11)**, 6024–6033, URL https://doi.org/10.1029/2019GL082850.

Nicholls, K. W., S. Østerhus, K. Makinson, T. Gammelsrød, and E. Fahrbach, 2009: Ice-ocean processes over the continental shelf of the southern Weddell Sea, Antarctica: A review. *Rev. Geophys.*, **47 (3)**, URL https://doi.org/10.1029/2007RG000250.

NOAA National Geophysical Data Center, 2009: ETOPO1 1 Arc-Minute Global Relief Model. *NOAA National Centers for Environmental Information*, URL https://doi.org/10.7289/V5C8276M.

Nøst, O. A., M. Biuw, V. Tverberg, C. Lydersen, T. Hattermann, Q. Zhou, L. H. Smedsrud, and K. M. Kovacs, 2011: Eddy overturning of the

Antarctic Slope Front controls glacial melting in the Eastern Weddell Sea. *J. Geophys. Res*, **116**, C11 014, URL https://doi.org/10.1029/2011JC006965.

Núñez-Riboni, I., and E. Fahrbach, 2009: Seasonal variability of the Antarctic Coastal Current and its driving mechanisms in the Weddell Sea. *Deep Sea Res. Part I*, **56 (11)**, 1927–1941, URL https://doi.org/10.1016/j.dsr.2009.06.005.

Padman, L., S. Y. Erofeeva, and H. A. Fricker, 2008: Improving Antarctic tide models by assimilation of ICESat laser altimetry over ice shelves. *Geophys. Res. Lett.*, **35 (22)**, URL https://doi.org/10.1029/2008GL035592.

Padman, L., H. A. Fricker, R. Coleman, S. Howard, and L. Erofeeva, 2002: A new tide model for the Antarctic ice shelves and seas. *Ann. Glaciol.*, **34**, 247–254, URL https://doi.org/10.3189/172756402781817752.

Powers, J. G., K. W. Manning, D. H. Bromwich, J. J. Cassano, and A. M. Cayette, 2012: A decade of Antarctic science support through AMPS. *Bull. Am. Meteorol. Soc.*, **93 (11)**, 1699–1712, URL https://doi.org/10.1175/BAMS-D-11-00186.1.

Powers, J. G., A. J. Monaghan, A. M. Cayette, D. H. Bromwich, Y.-H. Kuo, and K. W. Manning, 2003: Real-Time Mesoscale Modeling Over Antarctica: The Antarctic Mesoscale Prediction System* The Antarctic Mesoscale Prediction System. *Bull. Am. Meteorol. Soc.*, **84 (11)**, 1533–1546, URL https://doi.org/10.1175/BAMS-84-11-1533.

Robinson, I., 1981: Tidal vorticity and residual circulation. *Deep Sea Res. Part A*, **28 (3)**, 195–212, URL https://doi.org/10.1016/0198-0149(81)90062-5.

Rosenberg, M., and R. Gorton, 2019: BROKE West Survey, Marine Science Cruise AU0603 - Oceanographic Field Measurements and Analysis, Ver. 2. URL https://doi.org/10.26179/5ceb6d79c35a4.

Spall, M. A., and J. F. Price, 1998: Mesoscale variability in Denmark Strait: The PV outflow hypothesis. *J. Phys. Oceanogr.*, **28 (8)**, 1598–1623, URL https://doi.org/10.1175/1520-0485(1998)028<1598:MVIDST>2.0.CO;2.

St-Laurent, P., J. M. Klinck, and M. S. Dinniman, 2013: On the role of coastal troughs in the circulation of warm circumpolar deep water on Antarctic shelves. *J. Phys. Oceanogr.*, **43 (1)**, 51–64, URL https://doi.org/10.1175/JPO-D-11-0237.1.

Stern, A., L.-P. Nadeau, and D. Holland, 2015: Instability and mixing of zonal jets along an idealized continental shelf break. *J. Phys. Oceanogr.*, **45 (9)**, 2315–2338, URL https://doi.org/10.1175/JPO-D-14-0213.1.

Stern, A. A., A. Adcroft, and O. Sergienko, 2016: The effects of Antarctic iceberg calving-size distribution in a global climate model. *J. Geophys. Res.: Oceans*, **121 (8)**, 5773–5788, URL https://doi.org/10.1002/2016JC011835.

Stewart, A. L., and A. M. Hogg, 2017: Reshaping the Antarctic circumpolar current via Antarctic bottom water export. *J. Phys. Oceanogr.*, **47 (10)**, 2577–2601, URL https://doi.org/10.1175/JPO-D-17-0007.1.

Stewart, A. L., A. Klocker, and D. Menemenlis, 2019: Acceleration and overturning of the Antarctic Slope Current by winds, eddies, and tides. *J. Phys. Oceanogr.*, **49 (8)**, 2043–2074, URL https://doi.org/10.1175/JPO-D-18-0221.1.

Stewart, A. L., and A. F. Thompson, 2013: Connecting Antarctic cross-slope exchange with Southern Ocean overturning. *J. Phys. Oceanogr.*, **43 (7)**, 1453–1471, URL https://doi.org/10.1175/JPO-D-12-0205.1.

Stewart, A. L., and A. F. Thompson, 2015: Eddy-mediated transport of warm Circumpolar Deep Water across the Antarctic Shelf Break. *Geophys. Res. Lett.*, **42**, 432–440, URL https://doi.org/10.1002/2014GL062281.

Stewart, A. L., and A. F. Thompson, 2016: Eddy generation and jet formation via dense water outflows across the Antarctic continental slope. *J. Phys. Oceanogr.*, **46 (12)**, 3729–3750, URL https://doi.org/10.1175/JPO-D-16-0145.1.

Thompson, A. F., K. J. Heywood, S. Schmidtko, and A. L. Stewart, 2014: Eddy transport as a key component of the Antarctic overturning circulation. *Nat. Geosci.*, **7 (12)**, 879–884, URL https://doi.org/10.1038/ngeo2289.

Thompson, A. F., K. G. Speer, and L. M. Schulze Chretien, 2020: Genesis of the Antarctic Slope Current in West Antarctica. *Geophys. Res. Lett.*, **47 (16)**, e2020GL087 802, URL https://doi.org/10.1029/2020GL087802.

Thompson, A. F., A. L. Stewart, P. Spence, and K. J. Heywood, 2018: The Antarctic Slope Current in a changing climate. *Rev. Geophys.*, **56 (4)**, 741–770, URL https://doi.org/10.1029/2018RG000624.

Towns, J., and Coauthors, 2014: XSEDE: Accelerating scientific discovery. *Computing in Science & Engineering*, **16 (5)**, 62–74, URL https://doi.org/10.1109/MCSE.2014.80.

Tréguier, A.-M., and J. C. McWilliams, 1990: Topographic influences on wind-driven, stratified flow in a β-plane channel: An idealized model for the Antarctic Circumpolar Current. *J. Phys. Oceanogr.*, **20 (3)**, 321–343, URL https://doi.org/10.1175/1520-0485(1990)020<0321:TIOWDS>2.0.CO;2.

Tschudi, M., C. Fowler, J. Maslanik, J. S. Stewart, and W. N. Meier, 2016: Polar Pathfinder daily 25 km EASE-Grid Sea Ice motion vectors, version 3. *National Snow and Ice Data Center Distributed Active Archive Center, accessed February*, URL https://doi.org/10.5067/O57VAIT2AYYY.

Vallis, G. K., 2017: *Atmospheric and oceanic fluid dynamics*. Cambridge University Press, 136 pp., URL https://doi.org/10.1017/9781107588417.

Vancoppenolle, M., S. Bouillon, T. Fichefet, H. Goosse, O. Lecomte, M. Morales Maqueda, and G. Madec, 2012: The Louvain-la-Neuve sea ice model. *Notes du pole de modélisation, Institut Pierre-Simon Laplace (IPSL), Paris, France*, **(31)**, URL https://www.researchgate.net/publication/265061445.

Wang, Q., S. Danilov, and J. Schröter, 2009: Bottom water formation in the southern Weddell Sea and the influence of submarine ridges: Idealized numerical simulations. *Ocean Modell.*, **28 (1)**, 50–59, URL https://doi.org/10.1016/j.ocemod.2008.08.003.

Wang, Y., and A. L. Stewart, 2018: Eddy dynamics over continental slopes under retrograde winds: Insights from a model intercomparison. *Ocean Modell.*, **121**, 1–18, URL https://doi.org/10.1016/j.ocemod.2017.11.006.

Whitworth, T., III, A. H. Orsi, S.-J. Kim, W. D. Nowlin Jr, and R. A. Locarnini, 1985: Water masses and mixing near the Antarctic Slope Front. *Ocean, ice, and atmosphere: interactions at the Antarctic continental margin*, **75**, 1–27, URL https://doi.org/10.1029/AR075p0001.

Winton, M., 2000: A reformulated three-layer sea ice model. *J. Atmos. Oceanic Technol.*, **17 (4)**, 525–531, URL https://doi.org/10.1175/1520-0426(2000)017<0525:ARTLSI>2.0.CO;2.

Worby, A. P., C. A. Geiger, M. J. Paget, M. L. Van Woert, S. F. Ackley, and T. L. DeLiberty, 2008: Thickness distribution of Antarctic sea ice. *J. Geophys. Res.: Oceans*, **113 (C5)**, URL https://doi.org/10.1029/2007JC004254.

Zhang, J., and D. A. Rothrock, 2003: Modeling global sea ice with a thickness and enthalpy distribution model in generalized curvilinear coordinates. *Mon. Weather Rev.*, **131 (5)**, 845–861, URL https://doi.org/10.1175/1520-0493(2003)131<0845:MGSIWA>2.0.CO;2.

Zwally, H. J., J. C. Comiso, C. L. Parkinson, D. J. Cavalieri, and P. Gloersen, 2002: Variability of Antarctic sea ice 1979–1998. *J. Geophys. Res.: Oceans*, **107 (C5)**, 9–1, URL https://doi.org/10.1029/2000JC000733.